

COLLABORATIVE UAS CONTROL TO INCREASE
DECONFLICTION ABILITY IN THE NAS

Except where reference is made to the work of others, the work described in this thesis is my own or was done in collaboration with my advisory committee. This thesis does not include proprietary or classified information.

Brian C. Reitz

Certificate of Approval:

John E. Cochran Jr.
Professor and Head
Aerospace Engineering

Gilbert L. Crouse Jr., Chair
Associate Professor
Aerospace Engineering

Andrew J. Sinclair
Assistant Professor
Aerospace Engineering

George T. Flowers
Dean
Graduate School

COLLABORATIVE UAS CONTROL TO INCREASE
DECONFLICTION ABILITY IN THE NAS

Brian C. Reitz

A Thesis

Submitted to

the Graduate Faculty of

Auburn University

in Partial Fulfillment of the

Requirements for the

Degree of

Master of Science

Auburn, Alabama
August 10, 2009

COLLABORATIVE UAS CONTROL TO INCREASE
DECONFLICTION ABILITY IN THE NAS

Brian C. Reitz

Permission is granted to Auburn University to make copies of this thesis at its discretion, upon the request of individuals or institutions and at their expense. The author reserves all publication rights.

Signature of Author

Date of Graduation

VITA

Brian Christopher Reitz, son of Steven L. Reitz, Linda Ellen Cowall, and Debra Ann Reitz, was born August 14, 1985 in Columbus, Georgia. He graduated with honors from Russell County High School in Seale, AL, and entered Chattahoochee Valley Community College in the summer of 2003. After receiving his Associate of Science degree, he entered Auburn University in the spring of 2005. He graduated cum laude with a Bachelor of Aerospace Engineering degree in May of 2007, and entered Graduate School, Auburn University, the following semester.

THESIS ABSTRACT

COLLABORATIVE UAS CONTROL TO INCREASE
DECONFLICTION ABILITY IN THE NAS

Brian C. Reitz

Master of Science, August 10, 2009
(B.A.E., Auburn University, 2007)
(A.S., Chattahoochee Valley Community College, 2004)

111 Typed Pages

Directed by Gilbert L. Crouse Jr.

The progression of aviation has led to the strong desire to integrate unmanned aerial systems (UASs) into the national airspace system (NAS). In order for UASs to occupy the NAS concurrently with other aircraft, the Federal Aviation Administration (FAA) regulations require that UASs “see and avoid” (SAA) other air traffic to the same extent as a human pilot. The focus of this research is to explore the use of two collaborating unmanned aircraft working together to ensure separation from other air traffic using measurement data obtained from optical sensors. The system is designed for use with small, light-weight aircraft that are operated below 10,000 feet mean sea level. Computer simulation was used to explore the implementation of a control strategy for positioning the collaborating aircraft to maximize the accuracy of their estimates of interfering traffic locations and minimize the potential for conflicts while flying to a specified location. The performance of the range estimation algorithm was explored while subject to multiple interfering aircraft and operational constraints such as ownship maneuverability. A comparison with two other possible formations was

conducted to determine how the proposed method performed in both range estimate and miss distance of conflicting air traffic. The system reliability was also examined when faced with multiple types of target scenarios.

ACKNOWLEDGMENTS

The author would like to thank Dr. Gilbert L. Crouse Jr. for the opportunity to work on this research as well as his knowledge and invaluable support throughout the project. The author is appreciative of Dr. Crouse's belief in his abilities and guidance to become a young professional.

The author would also like to thank the Aerospace Engineering Department for its financial assistance and the Aerospace Engineering faculty for providing the knowledge to initially understand such a task. Dr. Andrew J. Sinclair was of great assistance in the acquisition of reference materials. The author also wishes to thank his colleague and friend, Jason Welstead, for his moral support and help with L^AT_EX. The author is perpetually thankful to his parents for their support and steadfast encouragement.

Finally, the author would like to dedicate this thesis to the memory of his grandfather, Mr. George Miller Reitz (March 19, 1931 - August 27, 1997.) Without this gentleman, the author's interest in aviation may have never been sparked. As the author continues his education, he will forever value the lessons learned from his grandfather.

Style manual or journal used American Institute of Aeronautics and Astronautics
(AIAA)

Computer software used MATLAB 2007a, Microsoft Office Word 2007, Microsoft
Office Excel 2007, Microsoft Paint, WinEdt, L^AT_EX

TABLE OF CONTENTS

LIST OF FIGURES	xi
LIST OF TABLES	xiii
1 INTRODUCTION	1
1.1 Performance Requirements	3
1.2 SAA System Overview	4
2 REVIEW OF LITERATURE	7
2.1 SAA Systems	7
2.2 Sensor Description	9
2.3 Range Detection	10
2.4 SAA System Decision	10
3 SYSTEM COMPARISON AND DISCUSSION	11
4 PLATFORM POSITIONING AND TARGET LOCALIZATION	14
4.1 Range Estimation Positioning	14
4.2 Measurement Platform Dynamics	17
4.3 Target Dynamics	18
4.4 Iterative EKF	19
4.5 Area of Uncertainty	23
4.6 Time to Closest Approach	25
4.7 Platform Positioning Controller	26
5 CONFLICT RESOLUTION	31
5.1 Conflict Geometry	32
5.2 Resolution Heading	33
5.3 Return to Initial Flight Path	37
5.4 Resolution Heading Maneuvering	38
6 SYSTEM IMPLEMENTATION	40
6.1 Optical Sensors	40
6.2 Target Recognition	41
6.3 Computational Processing	41
6.4 Weight Analysis	42

7	RESULTS	44
7.1	Alternative Systems	46
7.2	Comparison Target Scenario	47
7.3	Comparison Without Conflict Resolution	48
7.3.1	Range Error	49
7.3.2	Excess Distance Traveled	54
7.4	Conflict Resolution Algorithm Verification	56
7.5	Comparison With Conflict Resolution	61
7.5.1	Range Error	62
7.5.2	Excess Distance Traveled and Miss Distance	68
7.6	Affect of Platform Separation Distance	70
7.6.1	Range Error	71
7.6.2	Excess Distance Traveled and Miss Distance	74
7.7	Affect of UAS Performance Parameters	77
7.7.1	Range Error	77
7.7.2	Excess Distance Traveled and Miss Distance	80
7.8	Accuracy of Error Bounds	83
7.9	System Reliability	86
8	CONCLUSIONS	89
8.1	Comparison of Platform Separation Distances	89
8.2	Comparison of Performance Parameters	90
8.3	Error Bound Accuracy	90
8.4	System Reliability	91
9	FUTURE WORK	93
	BIBLIOGRAPHY	95

LIST OF FIGURES

1.1	Measurement Platform UAS with Sensors (Top, Front, and Side View).	5
2.1	TCAS System Diagram.	8
2.2	ADS-B Broadcast Service Architecture.	9
3.1	Researched SAA System Architecture.	12
3.2	Measurement UAS Maneuvering.	13
4.1	Optimal and Worst-case UAS Positioning for Range Estimation. . . .	15
4.2	UAS Formation Description.	16
4.3	Gaussian PDF With 90% Confidence Region.	25
4.4	Block Diagram of Measurement Platform Controller.	27
4.5	Block Diagram of PID Controller.	27
5.1	Geometry for Level Conflict Scenario.	32
5.2	Heading Changes to Resolve Conflict ($V_A > V_B$).	34
5.3	Heading Changes to Resolve Conflict ($V_A < V_B$).	35
5.4	Limiting Case for Two Solutions ($V_A < V_B$).	36
7.1	Three Platform Formation.	46
7.2	Constantly Rotating Two Platform Formation.	47
7.3	Comparison Scenario; Y-Axis Points North.	48
7.4	Average Range Error (Blue Line) and Standard Deviation (Red Line) for System 1.	50

7.5	Average Range Error (Blue Line) and Standard Deviation (Red Line) for System 2.	51
7.6	Average Range Error (Blue Line) and Standard Deviation (Red Line) for System 3.	52
7.7	Average Range Error Comparison.	55
7.8	First Four Verification Target Positions Traveling at 75 knots.	57
7.9	Last Four Verification Target Positions Traveling at 75 knots.	58
7.10	First Four Verification Target Positions Traveling at 125 knots.	59
7.11	Last Four Verification Target Positions Traveling at 125 knots.	60
7.12	Average Range Error (Blue Line) and Standard Deviation (Red Line) with Conflict Resolution for System 1.	63
7.13	Average Range Error (Blue Line) and Standard Deviation (Red Line) with Conflict Resolution for System 2.	64
7.14	Average Range Error (Blue Line) and Standard Deviation (Red Line) with Conflict Resolution for System 3.	65
7.15	Average Range Error Comparison with Conflict Resolution.	67
7.16	Average Range Error with 500 ft. Separation Distance.	71
7.17	Average Range Error with 1000 ft. Separation Distance.	72
7.18	Average Range Error with 1500 ft. Separation Distance.	73
7.19	Average Range Error Comparison with Varying Separation Distances.	75
7.20	Average Range Error with SEP of 500; ROT of 90 deg/min.	78
7.21	Average Range Error with SEP of 1500; ROT of 270 deg/min.	79
7.22	Average Range Error Comparison with Varying Performance Parameters.	81
7.23	Estimated Target Positions with Associated Area of Uncertainty.	83
7.24	Initial Estimated Target Position with Associated Area of Uncertainty for Target 3.	84
7.25	Range Estimate Histograms.	85
7.26	Multiple Target Near Miss Scenario.	88

LIST OF TABLES

6.1	Hardware Component Specifications.	42
6.2	Total System Weight and Power Required.	43
7.1	Specific Simulation Parameters.	45
7.2	Summary of Range Error Plots without Conflict Resolution.	53
7.3	Average Excess Distance Traveled and Standard Deviation for System 1.	54
7.4	Average Excess Distance Traveled and Standard Deviation for System 3.	56
7.5	Miss Distances for Verification Targets.	61
7.6	Summary of Range Error Plots with Conflict Resolution.	66
7.7	Average Excess Distance Traveled and Standard Deviation for System 1 with Conflict Resolution.	68
7.8	Average and Minimum Miss Distances and Standard Deviations for System 1 with Conflict Resolution.	68
7.9	Average and Minimum Miss Distances and Standard Deviations for System 2 with Conflict Resolution.	69
7.10	Average Excess Distance Traveled and Standard Deviation for System 3 with Conflict Resolution.	69
7.11	Average and Minimum Miss Distances and Standard Deviations for System 3 with Conflict Resolution.	70
7.12	Summary of Range Error Plots for Varying Separation Distances.	74
7.13	Average Excess Distance Traveled and Standard Deviation with a Sep- aration Distance of 500 ft.	75

7.14	Average and Minimum Miss Distances and Standard Deviations with a Separation Distance of 500 ft.	76
7.15	Average Excess Distance Traveled and Standard Deviation with a Separation Distance of 1500 ft.	76
7.16	Average and Minimum Miss Distances and Standard Deviations with a Separation Distance of 1500 ft.	76
7.17	Summary of Range Error Plots for Varying UAS Performance Parameters.	80
7.18	Average Excess Distance Traveled and Standard Deviation; SEP of 500, ROT of 90 deg/min.	80
7.19	Average and Minimum Miss Distances and Standard Deviations; SEP of 500, ROT of 90 deg/min.	81
7.20	Average Excess Distance Traveled and Standard Deviation; SEP of 1500, ROT of 270 deg/min.	82
7.21	Average and Minimum Miss Distances and Standard Deviations; SEP of 1500, ROT of 270 deg/min.	82

CHAPTER 1

INTRODUCTION

In the national airspace system (NAS), civil unmanned aerial systems (UASs) could perform tasks such as aerial geophysical surveys, low-level pipeline inspections, disaster monitoring, and forest-fire mapping [1]. Border surveillance, telecommunications relay services, and environmental monitoring are also missions that could be performed by civil UASs [2]. UASs could perform tasks in the NAS related to both military and commercial applications that would be infeasible or even impossible for manned aircraft. This is due in-part to their ability to stay aloft for long periods of time without concern for pilot fatigue as well as lower operating costs in some instances when compared to manned aircraft. Pilot safety is also a concern. UASs can do jobs that a human pilot cannot do safely.

Integrating UASs into the NAS comes with the challenge of avoiding midair collisions with other aircraft including non-cooperative piloted and non-piloted air vehicles. The Federal Aviation Administration’s (FAA) Aeronautical Information Manual (AIM) describes a near midair collision as: “an incident associated with the operation of an aircraft in which a possibility of collision occurs as a result of proximity of less than 500 feet to another aircraft” [3]. Non-cooperative aircraft would include aircraft without a transponder and ones operating without communicating with air traffic control. Federal Aviation Regulations (FARs) require that pilots “see and avoid” other aircraft when operating under visual flight rules (VFR) or when operating under instrument flight rules (IFR) in visual meteorological conditions (VMC) [4]. In congressional testimony the FAA’s Nick Sabatini said, “The extremely

broad range of unmanned aircraft make their successful integration into the national airspace system a challenge, but certainly one worth meeting” [5]. The Office of the Secretary of Defense (OSD) UAS Roadmap identifies the development of see and avoid (SAA) and collision avoidance systems as a critical technology goal [6].

Since UASs currently lack the ability to “see and avoid” other air traffic autonomously, military and government agency UAS operations in non-segregated airspace are limited under the Certificate of Waiver or Authorization (COA) process that requires operational restrictions to ensure that conflicts with other NAS users are limited. Civil unmanned aircraft have to go through a more difficult process to enter the NAS. Civil UAS users must obtain a Special Airworthiness Certificate in the Experimental Category and even then still face severe limitations on when, where, and how they can operate [7].

In order to operate freely in the NAS, unmanned aircraft must meet an “equivalent level of safety” (ELOS) to manned aircraft regarding the ability to see and avoid other aircraft [8]. The goal of the research described herein is to develop and simulate a system of two collaborating aircraft in which optical sensors are used to detect conflicting air traffic. By using two aircraft, a triangulated estimate of the traffic’s range is obtained. A control strategy is developed to maneuver the aircraft to optimize the range estimate. Successive range estimates and estimates of the traffic’s velocity are used to determine if the traffic is a collision hazard. If a hazard exists the controller maneuvers the aircraft to avoid any near midair collisions. Once the collision hazard is cleared the controller maneuvers the aircraft back to the original flight path and heading.

1.1 Performance Requirements

Performance requirements for SAA systems depend greatly on the size of the applicable UAS as well as the type of missions it is to accomplish while operating in the NAS. Smaller UASs have a substantially lower payload capability than their larger counterparts. Therefore, if a small UAS is to complete a mission in the NAS, the SAA system must be light-weight to allow for the addition of a payload. While larger UASs might effectively implement radar or other active scanning system to meet the requirements for operating UASs in the NAS, such a solution is problematic for smaller UASs because of their weight and power [9]. Solutions such as the Traffic alert and Collision Avoidance System (TCAS) and automatic dependent surveillance-broadcast (ADS-B) provide a method of sensing transponder equipped aircraft, however, due to weight and power constraints, most small UASs are not outfitted with such equipment. One solution to this size and weight constraint is through the use of optical sensors to sense interfering air traffic. Optical sensors are small, light-weight, and require little electrical power. On the other hand, optical sensors require processing power. With small, light-weight, optical sensors care has to be taken in the image resolution to efficiently detect traffic as early as possible to allow for ownship avoidance if the need arises. Title 14 Code of Federal Regulations (14 CFR) Part 91, section 91.117 dictates the maximum speed at which aircraft may be operated below 10,000 feet mean sea level as 250 knots [4]. With this speed restriction, research has shown that resolution requirements become less stringent [9]. A recommended instantaneous field of view per pixel for an avoidance maneuver with a 25° bank angle at 120 knots is 1.34 milliradians [9]. The instantaneous field of view per pixel is the camera field of view divided by the number of linear pixels in the focal plane [9]. Previous research has also determined that an appropriate Field of Regard (FOR) for the SAA

system should include airspace that lies within $\pm 110^\circ$ of the longitudinal axis of the aircraft and $\pm 15^\circ$ with respect to the vertical flight path [10]. With this FOR, a camera with at least 955 pixels in the horizontal plane is needed. 14 CFR Part 91, sections 91.111(a) and 91.113(b) are also important in the design of an SAA system because they describe how to operate near other aircraft as well as the right-of-way rules except water operations respectively [4]. The performance requirements for the designed system are to be light-weight and compact, have a FOR of at least $\pm 110^\circ$ in azimuth and $\pm 15^\circ$ in elevation, as well as follow all FARs.

1.2 SAA System Overview

The SAA approach presented here involves the use of two aircraft flying in formation nominally 1000 feet apart at the same altitude and heading. Each aircraft is equipped with three fixed optical sensors for traffic detection. The three sensors are placed on the airframe such that each sensor has a coverage area of ± 40 degrees in azimuth and ± 30 degrees in elevation. This is to ensure that the monitored azimuth covers $\pm 120^\circ$ of the longitudinal axis of each platform. With this coverage area, the FOR requirement mentioned in Section 1.1 will be exceeded. Figure 1.1 shows an example of the UAS and the field of view for each of the sensors.

Methods to detect a target in a digital image have been demonstrated by previous researchers [11, 12, 13, 14, 15]. Therefore, this research started with the assumption that a detection algorithm which provided azimuth and elevation measurements of the line of sight vector to the target was already available. It was also assumed that the sensors could detect the target perfectly. Another assumption made includes that of computational power. It was assumed that at least one of the UASs in the SAA system would either possess the equipment necessary to run the control algorithms

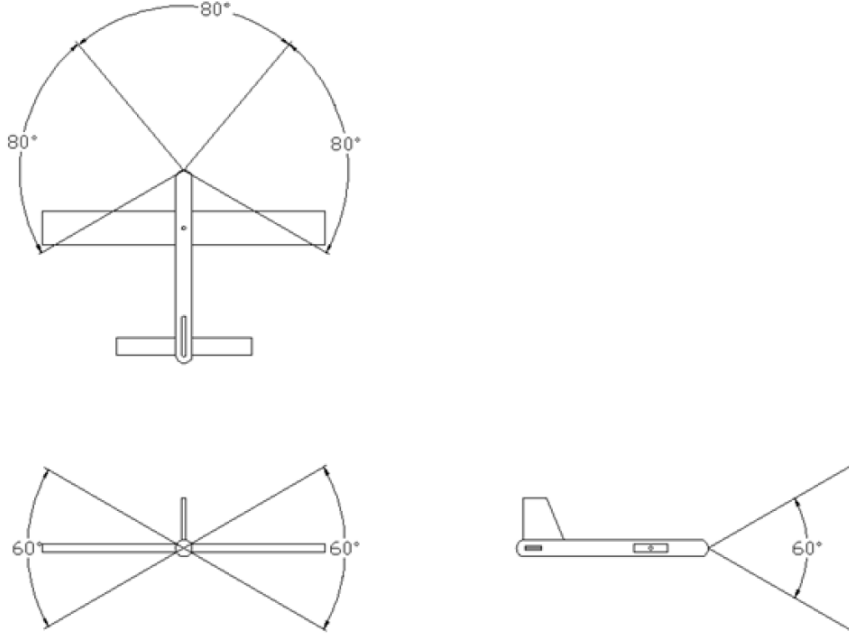


Figure 1.1: Measurement Platform UAS with Sensors (Top, Front, and Side View).

or it would possess the wireless capability to transmit and receive data at a rate high enough to use the output from algorithms implemented on a ground station. Also, the assumption that the UASs in the system could communicate with each other to relay information was made. With this foundation, the present research focused solely on the control algorithms along with the target position and velocity estimation.

Including the above assumptions, the system of UASs was simulated in a MATLAB environment. Various conflicting traffic flight paths were modeled with the target's motion assumed to follow a constant velocity trajectory. Simulated measurements at each time step (30 Hz) were generated based on the assumed trajectories. Zero-mean, Gaussian pseudorandom noise was then added to each of the measurements to simulate measurement uncertainty. Control of each of the measurement platforms was accomplished through the use of a proportional, integral, derivative

(PID) controller. The controller maneuvered the platform UASs to take more accurate measurements while also maneuvering them to avoid traffic conflicts.

CHAPTER 2

REVIEW OF LITERATURE

Research in the area of collision avoidance has been occurring since the mid 1950s when the FAA got involved after several mid-air collisions occurred where numerous people were killed [16]. With the modernization of the air traffic control system, the term conflict resolution, or deconfliction, has come about. The difference between collision avoidance and conflict resolution may first seem minuscule. In practice though the difference is quite important. Collision avoidance is an extreme maneuver performed at the last possible moment to avoid a collision. Conflict resolution, however, involves the careful planning of multiple flight tracks to avoid a collision avoidance situation.

2.1 SAA Systems

Many solutions to the collision avoidance and conflict resolution problem exist. Solutions such as various versions of the TCAS have been employed since the early 1980s. TCAS is an airborne system developed by the FAA that operates independently from the ground-based Air Traffic Control (ATC) system. It was designed to increase cockpit awareness of proximate aircraft and to serve as a “last line of defense” for the prevention of mid-air collisions [17]. Figure 2.1 shows a diagram of the TCAS system. More recently, the FAA, with the development of ADS-B, has offered another solution to the detection of conflicting air traffic. With ADS-B, both pilots and controllers can see radar-like displays with highly accurate traffic data that

update in real time and do not degrade with distance or terrain. The ADS-B system provides air-to-air surveillance as well as surveillance to remote or inhospitable areas that do not currently have coverage with radar [18]. Figure 2.2 shows a diagram of the ADS-B system architecture.

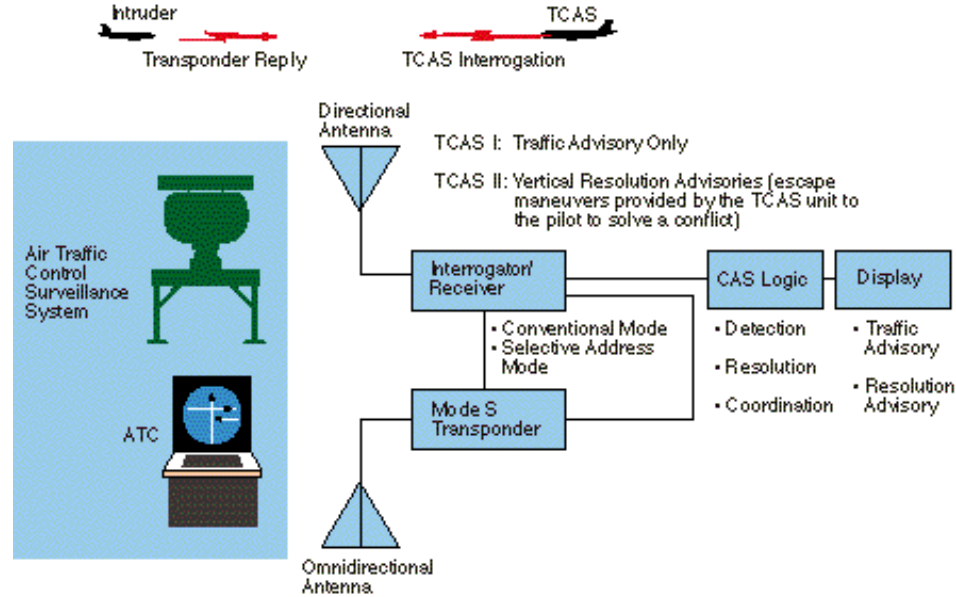


Figure 2.1: TCAS System Diagram [19].

Airborne radar has been in military use since World War II, when it was introduced to help night fighters locate bombers [16]. While the TCAS and ADS-B are both viable solutions for large transponder equipped aircraft, they are unable to detect non-cooperative aircraft. Radar, electro-optical, and infrared sensor systems are appealing solutions for detecting traffic because they do not require that other aircraft have special equipment. Passive systems such as electro-optical and infrared systems are attractive for unmanned aircraft since their power requirements and payload sizes would not accomodate radar systems [21].

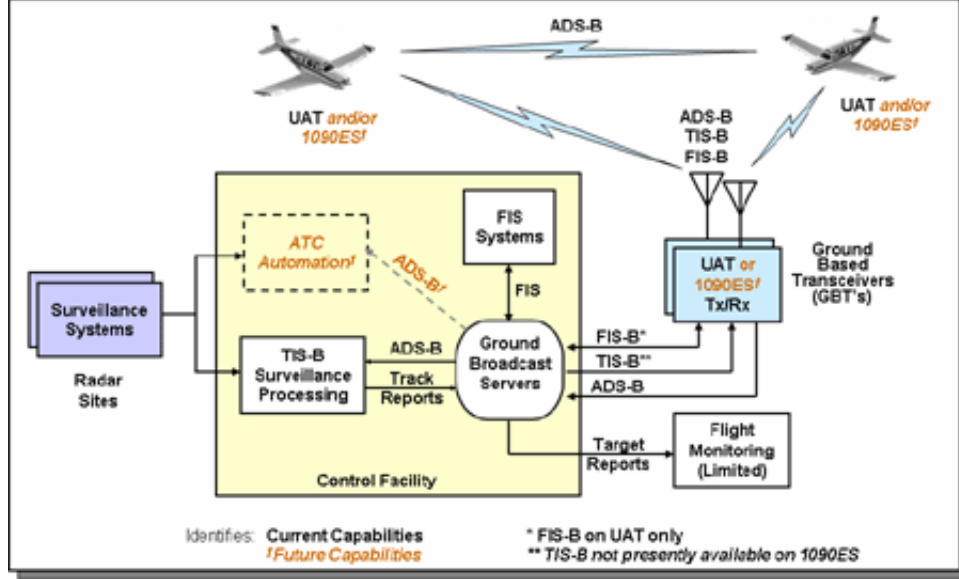


Figure 2.2: ADS-B Broadcast Service Architecture [20].

2.2 Sensor Description

Radar sensors work by emitting short pulses of radio waves created with a magnetron from an antenna. As the radio waves bounce off of other objects, they return to the antenna which doubles as a receiver when it is not transmitting. With the known direction of the antenna when the microwave was emitted and the time for the microwave to return, the range as well as direction to the target can be computed.

A passive sensor is a sensor designed to detect energy radiated or reflected from other objects. Passive sensors, unlike radar, do not emit energy themselves. Two types of common passive sensors are optical and infrared. An optical sensor detects light rays and converts them to an electric signal. An infrared sensor detects infrared radiation emitted from all objects in relation to their temperature. Both sensors compare the received energy with the previous, or standard, level of energy to detect an object. Since the sensors do not transmit energy themselves, the only information available is the direction from which the energy arrived.

2.3 Range Detection

Passive sensors work well for the detection of a collision hazard, but do not give very much information on where the target actually is or where it is going. O. Shakernia et al. employed the use of a small self maneuver to triangulate the position of the target after it has been detected [8]. Others have combined multiple types of sensors to detect and gather information on a collision hazard. G. Fasano et al. employed infrared sensors combined with radar to detect non-cooperative traffic [22]. The infrared sensors were used to detect conflicting traffic, and radar was used to gather information on the traffic's location and approximate velocity.

2.4 SAA System Decision

The main consideration as to the type of SAA system to incorporate on a particular UAS depends on its size, weight, mission, and payload capability. Currently there are no laws or FARs governing the type of SAA system UASs must use. The FAA's main concern with UASs operating in the NAS is safety. The FAA, in 2005, asked the Radio Technical Commission for Aeronautics (RTCA), a group that frequently advises the agency on technical issues, to help develop standards for UAS SAA systems [23]. The RTCA committee for UASs, SC-203, has been asked to produce Minimum Aviation System Performance Standards (MASPS) for SAA systems to be employed on UASs operating in the NAS by fiscal year 2011 [24].

CHAPTER 3

SYSTEM COMPARISON AND DISCUSSION

Until recently, most of the SAA solutions available were extremely heavy or bulky. This is in part due to the fact that most of the systems available were developed for large manned aircraft. With UASs becoming a more viable solution for some missions, a compact and light-weight solution is needed. Systems with multiple sensor types are satisfactory for some applications, but the complexity of these systems make them unsuitable for use on small UASs.

A diagram of the proposed SAA system can be seen in Figure 3.1. As can be seen in the illustration, the SAA system includes the use of two UASs each equipped with optical sensors for target detection. Since the system only employs the use of one type of sensor, there is an advantageous decrease in the system weight carried by the UASs. Optical sensors are incorporated to decrease the system size and complexity as opposed to carrying radar sensing equipment. Two UASs are employed to triangulate the position of the target to address the range detection problem with optical sensors mentioned previously. Using two UASs to triangulate the position also addresses the issue of time with respect to an accurate estimation in target location. In the method mentioned in Section 2.3 where a small self maneuver is used to triangulate the target's position, an increase in the time required to accurately estimate the target's position is incurred. This time is important because the aircraft has to detect the traffic with enough time remaining before collision to execute an avoidance maneuver and maintain the required separation distance.

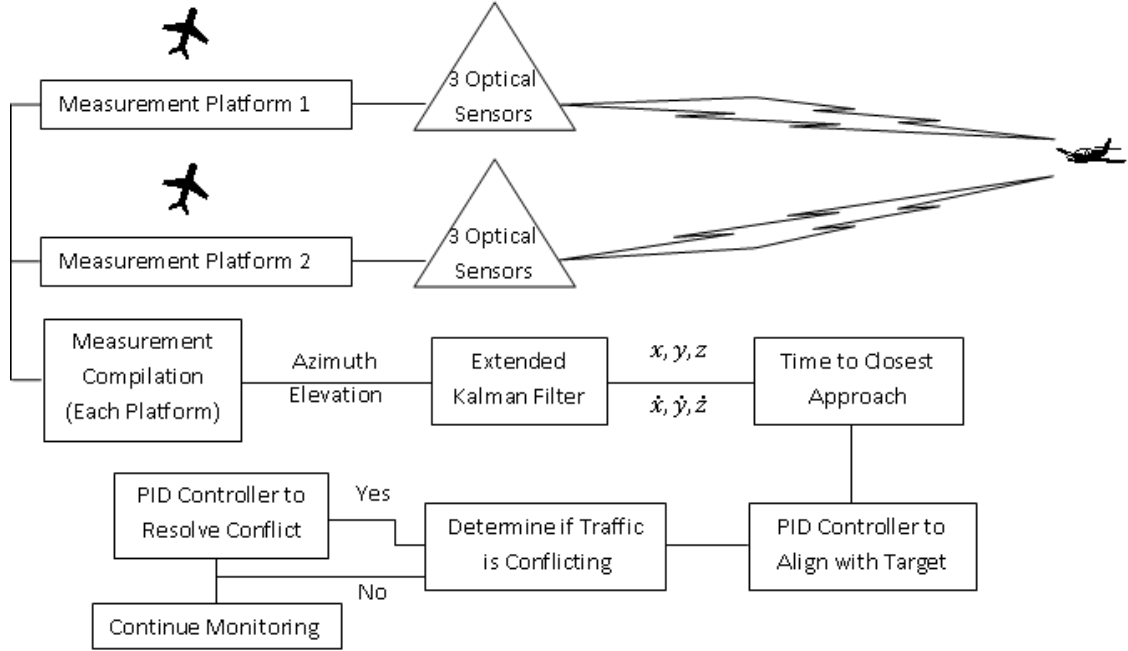


Figure 3.1: Researched SAA System Architecture.

Measurements from the sensors on-board each UAS are used in conjunction with an iterative extended Kalman filter (EKF) to estimate the state for each of the observable targets. After each target's state is estimated, the area of uncertainty associated with the estimate is calculated from the estimated covariance. The time to closest approach, t_{ca} , for each of the targets is also calculated from the state estimate. Based on this t_{ca} , the system determines which target needs to have more accurate measurements. A PID controller then aligns the UASs to take those measurements. The more accurate measurements are obtained by aligning the UASs perpendicular to the line of sight vector to the traffic. Using the estimated target position and velocity, the system determines if there will be a traffic conflict. If so, a PID controller maneuvers the UASs to avoid that conflict. If no conflict exists, the UASs continue on their assigned flight path.

The orientation of the measurement UASs is based off of a circle. During maneuvering, the UASs are held at a fixed distance apart. To maneuver, the UASs simply rotate about the center point of the formation. Figure 3.2 depicts how the UASs maneuver to provide more accurate measurements to the target state estimator.

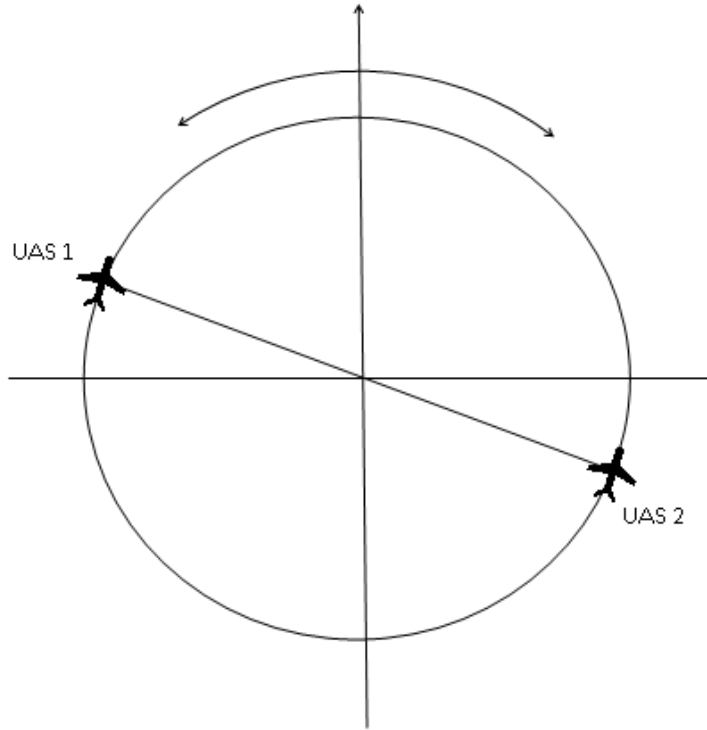


Figure 3.2: Measurement UAS Maneuvering.

Since the UAS system geometry is based off of a circle it is easy to control the system to maneuver away from conflicting traffic. The heading of the center point for the circle is simply commanded to change. This system geometry coupled with the target estimator simplifies conflicting traffic position estimation as well as conflict resolution.

CHAPTER 4

PLATFORM POSITIONING AND TARGET LOCALIZATION

In the previous chapter, methods for positioning the UAS platforms for target localization were introduced. Presented now is an in-depth description of the mathematical method for performing those tasks.

4.1 Range Estimation Positioning

Since the optical sensors provide only azimuth and elevation to the target, range cannot be directly measured by a single measurement platform UAS. However, by working collaboratively, the two UASs are able to triangulate the position of the traffic. The accuracy of that position estimate depends on the relative position of the target to the measurement aircraft. To obtain an optimal range estimate or the best range estimate for the formation, the two aircraft are positioned perpendicular to the line joining the traffic and the mean of the two aircraft's positions. On the other hand, if they are positioned parallel to that line, no range information can be deduced as illustrated in Figure 4.1. In the figure, and for the remainder of this thesis, the word optimal is used to refer to the position of the aircraft in the defined formation in which the best range estimate is obtained.

Initially, and anytime there are no targets in the FOR of the measurement aircraft, the UASs are configured to fly abreast at the same altitude. The angle of the platforms, aop , and the separation distance, $sepdist$, are the two parameters that describe the aircraft formation. Figure 4.2 illustrates these parameters. The angle of

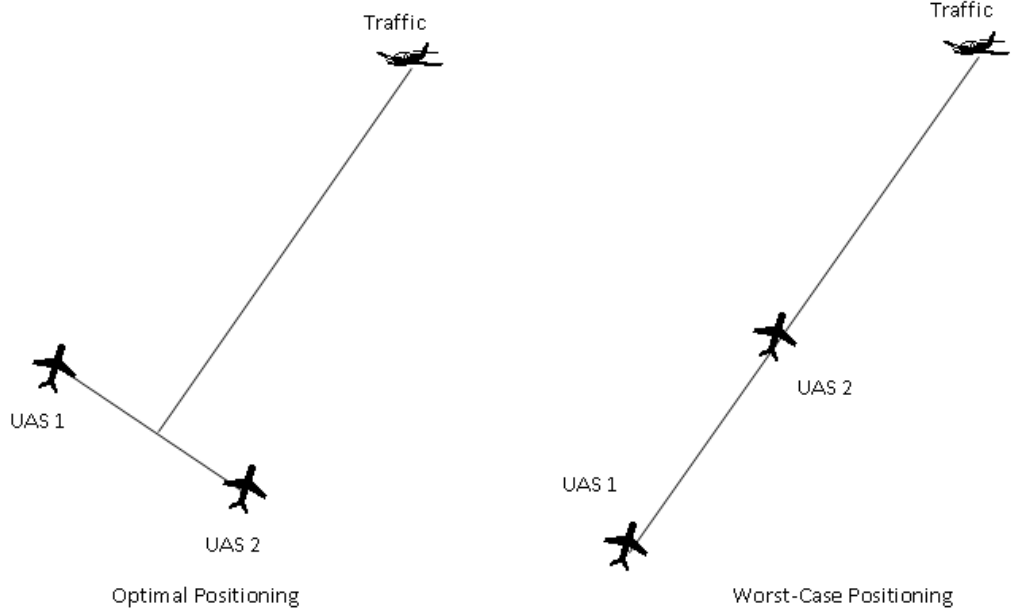


Figure 4.1: Optimal and Worst-case UAS Positioning for Range Estimation.

the platforms is calculated using Equation (4.1) and is based off of the target location as well as the center location of the measurement aircraft system. Equation (4.2) describes how the position of each measurement aircraft is found from the angle of the platforms.

$$aop_{opt} = \tan^{-1} \left(\frac{y_t - y_c}{x_t - x_c} \right) \quad (4.1)$$

$$\begin{aligned} x_1 &= x_c + \frac{sepdist}{2} \sin(aop_{opt}) \\ y_1 &= y_c + \frac{sepdist}{2} \cos(aop_{opt}) \\ x_2 &= x_c - \frac{sepdist}{2} \sin(aop_{opt}) \\ y_2 &= y_c - \frac{sepdist}{2} \cos(aop_{opt}) \end{aligned} \quad (4.2)$$

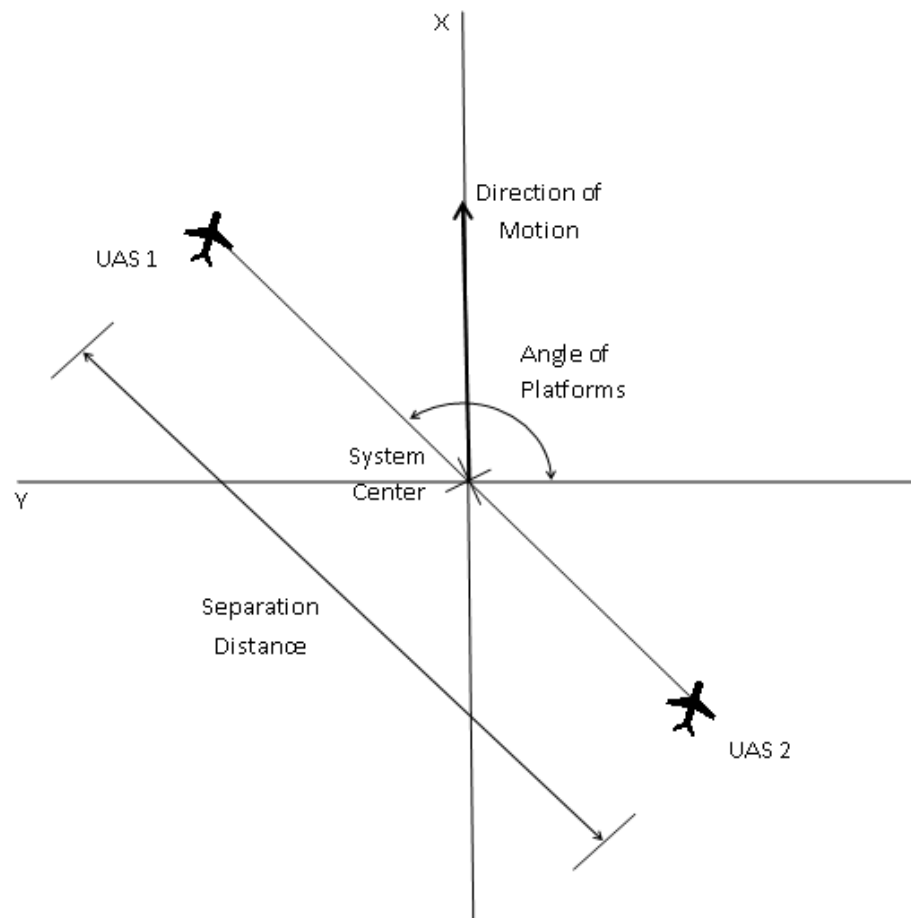


Figure 4.2: UAS Formation Description.

4.2 Measurement Platform Dynamics

Each UAS, or measurement platform, was modeled as a point mass that traveled with constant acceleration. Equation (4.3) describes the dynamics of the measurement platforms.

$$\dot{X} = AX + BU \quad (4.3)$$

Equation (4.4) describes the state of the measurement platforms and Equation (4.5) describes the state matrix.

$$X = \begin{bmatrix} x \\ \dot{x} \\ y \\ \dot{y} \\ z \\ \dot{z} \end{bmatrix} \quad (4.4)$$

$$A = \begin{bmatrix} 0 & 1 & 0 & 0 & 0 & 0 & 0 & 0 & 0 \\ 0 & 0 & 1 & 0 & 0 & 0 & 0 & 0 & 0 \\ 0 & 0 & 0 & 0 & 1 & 0 & 0 & 0 & 0 \\ 0 & 0 & 0 & 0 & 0 & 1 & 0 & 0 & 0 \\ 0 & 0 & 0 & 0 & 0 & 0 & 0 & 1 & 0 \\ 0 & 0 & 0 & 0 & 0 & 0 & 0 & 0 & 1 \end{bmatrix} \quad (4.5)$$

Equations (4.6) describe B and U from Equation (4.3).

$$B = \begin{bmatrix} 0 & 0 & 0 \\ 1 & 0 & 0 \\ 0 & 0 & 0 \\ 0 & 1 & 0 \\ 0 & 0 & 0 \\ 0 & 0 & 1 \end{bmatrix} \quad (4.6)$$

$$U = \begin{bmatrix} \ddot{x} \\ \ddot{y} \\ \ddot{z} \end{bmatrix}$$

Here, the x , y , and z directions correspond with a East, North, and Up coordinate system.

4.3 Target Dynamics

In the present research, the target's motion was assumed to follow a constant velocity trajectory. The filter state, X , includes the three-dimensional vector location and velocity for the target in world coordinates as shown in Equation (4.7).

$$X = \begin{bmatrix} x \\ \dot{x} \\ y \\ \dot{y} \\ z \\ \dot{z} \end{bmatrix} \quad (4.7)$$

The state transition matrix for the target's motion is shown in Equation (4.8).

$$\Phi = \begin{bmatrix} 1 & dt & 0 & 0 & 0 & 0 \\ 0 & 1 & 0 & 0 & 0 & 0 \\ 0 & 0 & 1 & dt & 0 & 0 \\ 0 & 0 & 0 & 1 & 0 & 0 \\ 0 & 0 & 0 & 0 & 1 & dt \\ 0 & 0 & 0 & 0 & 0 & 1 \end{bmatrix} \quad (4.8)$$

4.4 Iterative EKF

To estimate the position of potentially conflicting traffic, a Kalman filter based state estimator was developed. The Kalman filter is a set of mathematical equations that provide an efficient computational (recursive) means to estimate the state of a process, in a way that minimizes the mean of the squared error [25]. Since a Kalman filter addresses the general problem of estimating the state of a discrete-time controlled process that is governed by a linear stochastic difference equation and our measurements are non-linear some modifications had to be made. A Kalman filter that linearizes about the current mean and covariance is referred to as an extended Kalman filter or EKF [25].

For this work, an iterative EKF was developed to accept the azimuth and elevation measurements generated and estimate the state of the target from those measurements. The iterated EKF is the same as the EKF with the addition of a tolerance on the state estimation. The filter iterates the state estimate until the specified error tolerance between the projected estimate of the state and the filter state estimate is reached.

The measurements are generated each time step by first calculating the true azimuth and elevation from the known position of both the measurement platforms and the true flight track of the target. Zero-mean, Gaussian pseudorandom noise with a standard deviation, r , of $\frac{1}{4}^\circ$ was then added to each of the measurements to simulate measurement uncertainty. This value corresponds to an error in target detection of three pixels in the camera FOV. Equations (4.9) show how the azimuth and elevation measurements, Az_{meas} and El_{meas} , for each platform are calculated. For the performed simulations presented later, the FOV for each sensor was unlimited.

$$\begin{aligned}
Az_{meas_{mp1}} &= Az_{true_{mp1}} + r * randn \\
El_{meas_{mp1}} &= El_{true_{mp1}} + r * randn \\
Az_{meas_{mp2}} &= Az_{true_{mp2}} + r * randn \\
El_{meas_{mp2}} &= El_{true_{mp2}} + r * randn
\end{aligned} \tag{4.9}$$

Estimating the state with a Kalman filter occurs in two steps. First, the filter projects the current state and error covariance forward in time. This is known as the “time update.” Equations (4.10) are the time update equations for the state and error covariance.

$$\begin{aligned}
X_k^- &= \Phi X_{k-1} \\
P_k^- &= \Phi P_{k-1} \Phi^T + Q
\end{aligned} \tag{4.10}$$

Next, feedback on the estimate is obtained through measurements. The previously correlated measurements of azimuth and elevation from each platform are incorporated into the projected state estimate to obtain an improved estimate. This second portion of the filter is known as the “measurement update.” Equations (4.11) are the

measurement update equations.

$$\begin{aligned}
K &= P_k^- H^T (H P_k^- H^T + R)^{-1} \\
P_k &= (I - KH) P_k^- \\
X_k &= X_k^- + P_k H^T R^{-1} (z_k - h)
\end{aligned} \tag{4.11}$$

Process or plant noise, Q , was added to the error covariance, P_k^- , to allow for minor disturbances in position and velocity as well as to allow the estimator to adapt to target maneuvers. The amount of process noise needed depends on the convergence rate of the estimated state to the value of the true state. The process noise can be increased slightly to speed up the convergence rate. There is a limit, however, on the amount of noise added. Too much process noise can cause oscillations in the state estimate and the estimate will never fully converge to the actual value.

The updated state estimate and error covariance in Equation (4.11) include the Kalman gain, K , as well as H which relates the state to the measurement, z . For the EKF, H is the Jacobian matrix of partial derivatives of h with respect to the state as shown in Equation (4.12).

$$H_{[i,j]} = \frac{\partial h_{[i]}}{\partial x_{[j]}} (\tilde{x}_k, 0) \tag{4.12}$$

Equation (4.13) represents h , or the measurements of azimuth, Az , and elevation, El , from each of the two measurement platforms.

$$h = \begin{bmatrix} Az_{mp1} \\ El_{mp1} \\ Az_{mp2} \\ El_{mp2} \end{bmatrix} \tag{4.13}$$

where

$$\begin{aligned}
Az_{mp1} &= \tan^{-1} \frac{x - x_{pltfm1}}{y - y_{pltfm1}} \\
El_{mp1} &= \tan^{-1} \frac{z - z_{pltfm1}}{Rg1} \\
Az_{mp2} &= \tan^{-1} \frac{x - x_{pltfm2}}{y - y_{pltfm2}} \\
El_{mp2} &= \tan^{-1} \frac{z - z_{pltfm2}}{Rg2}
\end{aligned} \tag{4.14}$$

and

$$\begin{aligned}
Rg1 &= \sqrt{(x - x_{pltfm1})^2 + (y - y_{pltfm1})^2} \\
Rg2 &= \sqrt{(x - x_{pltfm2})^2 + (y - y_{pltfm2})^2}
\end{aligned} \tag{4.15}$$

R in the measurement update equations is the measurement noise covariance matrix derived from the estimated position and orientation uncertainty of the measurement platforms used in the measurement model. Equation (4.16) represents the measurement noise covariance matrix, R where r is the same as in Equations (4.9) above.

$$R = \begin{bmatrix} r^2 & 0 & 0 & 0 \\ 0 & r^2 & 0 & 0 \\ 0 & 0 & r^2 & 0 \\ 0 & 0 & 0 & r^2 \end{bmatrix} \tag{4.16}$$

In the SAA system, each target in the FOR of the measurement platforms was assigned a separate filter. Each filter was initialized based on the measurements of azimuth and elevation to that target as well as the known location of both measurement UASs. Each target's filter received the same initial conditions for velocity and error covariance. The initial velocity estimate was set to zero and the initial error

covariance was set high so that the filter would rely more on the measurements than the initial state estimate for the first filter iteration.

4.5 Area of Uncertainty

In addition to the state estimate for each target in the UAS's FOR, the area of uncertainty for the estimate was calculated along the target's estimated flight track. This was accomplished through the error covariance matrix that was calculated in the EKF. The error covariance matrix that was output by the EKF was a 6×6 matrix that described how the state variables influenced each other. Equation (4.17) represents the error covariance matrix.

$$P = \begin{bmatrix} \sigma_x^2 & \sigma_{x\dot{x}} & \sigma_{xy} & \sigma_{x\dot{y}} & \sigma_{xz} & \sigma_{x\dot{z}} \\ \sigma_{\dot{x}x} & \sigma_{\dot{x}}^2 & \sigma_{\dot{x}y} & \sigma_{\dot{x}\dot{y}} & \sigma_{\dot{x}z} & \sigma_{\dot{x}\dot{z}} \\ \sigma_{yx} & \sigma_{y\dot{x}} & \sigma_y^2 & \sigma_{y\dot{y}} & \sigma_{yz} & \sigma_{y\dot{z}} \\ \sigma_{\dot{y}x} & \sigma_{\dot{y}\dot{x}} & \sigma_{\dot{y}y} & \sigma_{\dot{y}}^2 & \sigma_{\dot{y}z} & \sigma_{\dot{y}\dot{z}} \\ \sigma_{zx} & \sigma_{z\dot{x}} & \sigma_{zy} & \sigma_{z\dot{y}} & \sigma_z^2 & \sigma_{z\dot{z}} \\ \sigma_{\dot{z}x} & \sigma_{\dot{z}\dot{x}} & \sigma_{\dot{z}y} & \sigma_{\dot{z}\dot{y}} & \sigma_{\dot{z}z} & \sigma_{\dot{z}}^2 \end{bmatrix} \quad (4.17)$$

The error covariance matrix can be broken up into three 2×2 matrices, represented by Equations (4.18), where each one describes the area of uncertainty in a

separate two-dimensional coordinate frame.

$$\begin{aligned}
P_{xy} &= \begin{bmatrix} \sigma_x^2 & \sigma_{xy} \\ \sigma_{yx} & \sigma_y^2 \end{bmatrix} \\
P_{xz} &= \begin{bmatrix} \sigma_x^2 & \sigma_{xz} \\ \sigma_{zx} & \sigma_z^2 \end{bmatrix} \\
P_{yz} &= \begin{bmatrix} \sigma_y^2 & \sigma_{yz} \\ \sigma_{zy} & \sigma_z^2 \end{bmatrix}
\end{aligned} \tag{4.18}$$

The area of uncertainty is the area inside an error ellipse that is centered at the target location estimate. Therefore, to calculate the area of uncertainty, the composition of an ellipse must be understood. Every ellipse is defined by two axes, a semi-major axis and a semi-minor axis. The two things that are needed to determine the size of an ellipse are the magnitude and direction of each axis. To obtain these values, the eigenvectors and eigenvalues for each of the 2×2 error covariance matrices in Equations (4.18) were calculated. The eigenvectors specify the direction of the ellipse axes while the square roots of the eigenvalues give the magnitude.

All error ellipses have an associated confidence factor. The confidence bound for the area of uncertainty in the SAA system was set to 74% due to the two variables with which each ellipse was plotted. This confidence bound describes the probability that the true position of the target will be located in the confidence area and was used for visualization of the filter estimate. Since the measurements are assumed to contain Gaussian noise with zero-mean, the confidence factor for the error ellipses was determined by using a standard normal distribution table. Figure 4.3 illustrates

a Gaussian probability density function (PDF) for a single variable with a 90% confidence region and the confidence factor of 1.645. For two variables, this confidence factor relates to a 74% confidence region.



Figure 4.3: Gaussian PDF With 90% Confidence Region.

4.6 Time to Closest Approach

For each target being tracked, their time to closest approach, t_{ca} , was calculated. The time to closest approach is the time at which the traffic would be within minimum range if the speed and heading of both the platforms and the target remain constant. The first step in this calculation is to find the relative position vector from the measurement UASs to each target at an arbitrary time, t . The relative position vector, \vec{r} , is defined as the difference between the position vector to the measurement platform UASs in world coordinates, \vec{r}_p , and the position vector to the target in world coordinates, \vec{r}_t , and is shown in Equation (4.19).

$$\vec{r} = \vec{r}_p - \vec{r}_t \quad (4.19)$$

Equations (4.20) and (4.21) describe the position vector to the measurement platforms and the position vector to the target respectively.

$$\vec{r}_p = \vec{r}_{p0} + \vec{v}_p t \quad (4.20)$$

$$\vec{r}_t = \vec{r}_{t0} + \vec{v}_t t \quad (4.21)$$

To solve for the time to closest approach, the magnitude of the relative position vector, $|\vec{r}|$, must be differentiated with respect to time, t , and set equal to zero as in Equation (4.22). With the magnitude of the relative position vector, the time to closest approach is represented as a function of measurement platform position and velocity as well as the position and velocity of the target as can be seen in Equation (4.23).

$$\frac{\partial |\vec{r}|}{\partial t} = 0 \quad (4.22)$$

$$t_{ca} = \frac{-(\vec{v}_p - \vec{v}_t) \cdot (\vec{r}_p - \vec{r}_t)}{|\vec{v}_p - \vec{v}_t|^2} \quad (4.23)$$

4.7 Platform Positioning Controller

Once the optimal location of each aircraft for taking measurements is known from Equation (4.2) as well as a conflict resolution heading discussed in the next chapter, a PID controller is used to maneuver the aircraft to that location. The two aircraft in the system are each assigned a controller. A block diagram of the platform controller is shown in Figure 4.4

A PID controller corrects errors between a measured process variable, in this case the location of the aircraft, and a desired variable, where the aircraft needs to

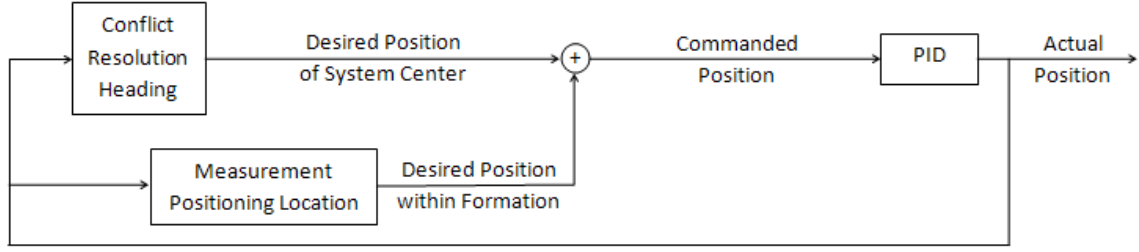


Figure 4.4: Block Diagram of Measurement Platform Controller.

be to take optimal measurements, by outputting a corrective action. The controller has three elements that determine the corrective action. A block diagram of a PID controller is shown in Figure 4.5 where t here represents time. A brief description of each element, or block in the illustration, of the controller accompanies the figure [26].

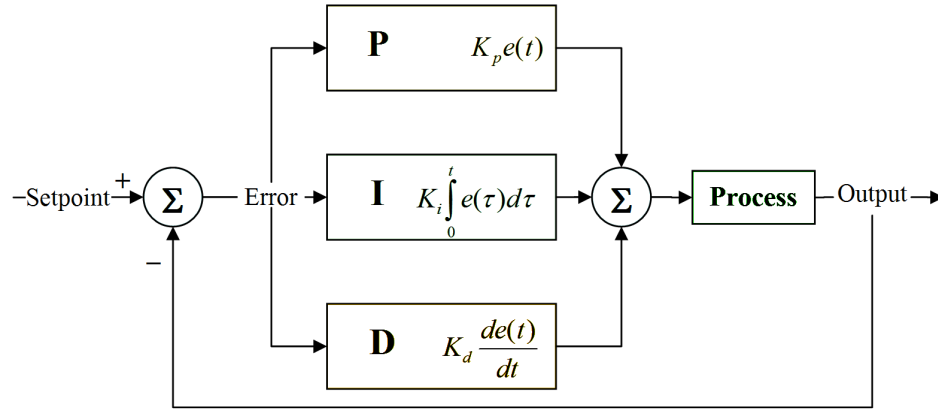


Figure 4.5: Block Diagram of PID Controller.

(P) **Proportional Block:** The proportional block of the controller determines the reaction of the process to the current error, e . In this case, the error is the distance between where the aircraft is and where it needs to be. K_p in Figure 4.5 is the proportional gain. The proportional block makes a change to the controller output that is proportional to the current error value.

(I) **Integral Block:** The integral block of the controller determines the process' reaction based on the summation of recent errors. The integral block is used to add long-term precision to the controller. K_i in Figure 4.5 is the integral gain. The integral term, when added to the proportional term, eliminates the residual steady-state error associated with a proportional only controller. The output from the integral block is proportional to both the magnitude of the error and the duration of the error.

(D) **Derivative Block:** The derivative block determines the reaction of the process based on the rate at which the error has been changing. The derivative term accelerates the rate of change of the controller output. K_d in Figure 4.5 is the derivative gain.

The corrective output from the PID controller for each aircraft is a sequence of acceleration commands that should maneuver the aircraft to the desired location. The controller up-date rate was 30 Hertz. Each time step, the current position as well as the desired position from Equation (4.2) was known. The difference between the two values was the error in the controller.

The acceleration values in the controller were limited by maximum and minimum values to simulate the desired flight characteristics of the measurement aircraft. Assuming the platforms are traveling East, the longitudinal acceleration limits, in the direction of the velocity, were determined by the specific excess power, SEP , which is the difference between the power available and the power required for the aircraft. The lateral acceleration limits, in the Y direction assuming an Easterly heading, were determined by the maximum rate of turn for the aircraft, ROT_{max} , as well as the separation distance, $sepdist$, between the two measurement aircraft. Equations (4.24) show how each of these limits were calculated. V_c is the measurement platform cruise

speed and g is the acceleration of gravity.

$$\begin{aligned}
\ddot{x}_{max} &= SEP \frac{g}{V_c} \\
\ddot{x}_{min} &= -X_{accmax} \\
\ddot{y}_{max} &= \frac{sepdist}{2} ROT_{max}^2 \\
\ddot{y}_{min} &= -Y_{accmax}
\end{aligned} \tag{4.24}$$

Another limit in the controller was on the integrator state. To keep the integrator state from growing or shrinking to very large values, maximum and minimum bounds on the error summation were incorporated. When the integrator state, the error summation, gets large it results in integrator windup. In an integrator windup situation, the controller plant would have reached the target, but the integrator value would still be large. The integral block would then cause the output to go beyond the desired value while the integrator unwinds and the process reverses.

In order to insure that the controller would give a stable output, the controller gains, K_p , K_i , and K_d , had to be “tuned.” There are several methods for tuning a PID controller. The method chosen is known as the Ziegler-Nichols method introduced by John G. Ziegler and Nathaniel B. Nichols [26]. This method was chosen because it is a proven and accurate means for determining controller gains. First, the integral and derivative gains are set to zero so that the controller only consists of the proportional block. Then, through iterations with the filter, the proportional gain is increased until it reaches the critical gain, K_c . With this gain in the proportional block only, the output of the controller causes the aircraft’s position to oscillate. The method then describes the controller gains as functions of the critical gain and the oscillation period, P_c . Equation (4.25) shows how the controller gains are functions of the critical

gain and the oscillation period.

$$\begin{aligned} K_p &= 0.6K_c \\ K_i &= \frac{2K_p}{P_c} \\ K_d &= \frac{K_p P_c}{8} \end{aligned} \tag{4.25}$$

For this system the critical gain was found to be two and the corresponding oscillation period was 100 seconds. With these values the gains were set to 1.2, 0.024, and 15 for the proportional gain, K_p , the integral gain, K_i , and the derivative gain, K_d respectively.

CHAPTER 5

CONFLICT RESOLUTION

The purpose for this SAA system is to give UASs deconfliction ability while operating in the NAS. For UASs, one problem comes with their interaction with human pilots. A collision avoidance algorithm, while it may meet certain separation criteria, could give human pilots uncertainty as to when, how, or even if the UAS is going to respond to a traffic conflict. With a conflict resolution algorithm, that uncertainty can be minimized by performing a resolution maneuver well before the conflicting traffic is at its minimum separation distance.

For this system, a geometric approach to conflict resolution was employed. Papers by K. Bilimoria and R. Paielli review the literature on this topic and present useful results [27, 28]. The method described by R. Bach et al. for level aircraft conflict resolution was incorporated for conflict detection and resolution [29]. The deconfliction algorithm makes adjustments to the measurement platform's heading to resolve conflicts with other air traffic as they are detected. The algorithm created differs from the one mentioned above in the method used to determine if the traffic is no longer a conflict. In Bach's paper a distance and time to turn back are calculated. For this work, the geometry was used to determine if the traffic was no longer a conflict. Once it was determined that the traffic was no longer a conflict, the measurement platforms were commanded to return to their original flight path and heading by an intercept angle that was determined from the distance the platforms deviated.

5.1 Conflict Geometry

To define the conflict geometry, a circle with radius equal to that of the minimum allowable separation distance is first created around the traffic in question. For this work the minimum allowable separation distance was set to 1000 feet which exceeds the AIM's definition of avoiding a near midair collision. This radius, R_{ms} , along with the speed and heading for each aircraft and the range to the traffic, S_0 , describe the geometry as shown in Figure 5.1 where A is the center of the measurement platforms and B is the traffic. C in the figure depicts the corner of the velocity triangle of the measurement platforms and the conflicting traffic. In the world coordinate system in the figure, the x -axis is defined as East and the y -axis is North.

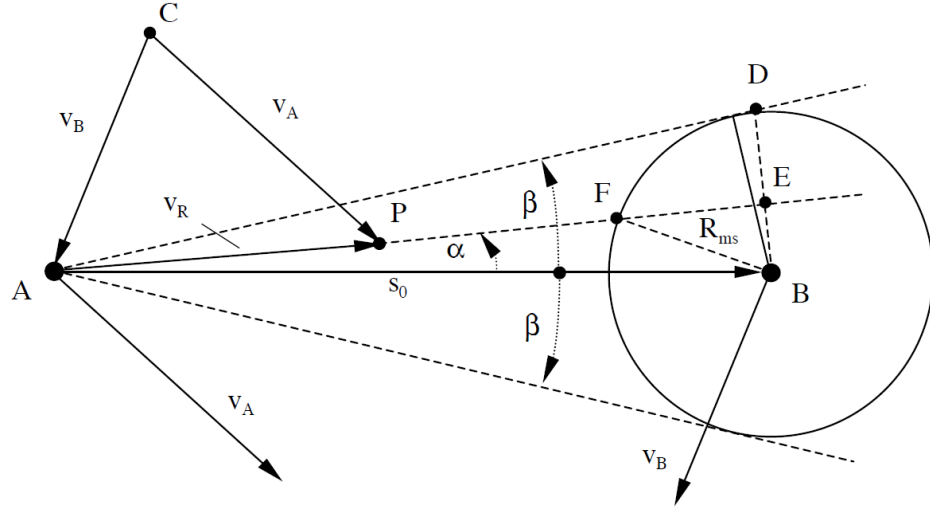


Figure 5.1: Geometry for Level Conflict Scenario [29].

From the EKF mentioned in Section (4.4) the estimated position and velocity of the traffic is known. This information gives the range to the target as well as the target heading. The angle β between the dashed lines tangent to the minimum

separation circle and the range vector was calculated from Equation (5.1) [29].

$$\beta = \pm \sin^{-1} \left(\frac{R_{ms}}{S_0} \right) \quad (5.1)$$

The angle α between the range vector and the relative velocity vector was calculated using Equation (5.2)

$$\alpha = \psi_r - \psi_0 \quad (5.2)$$

where ψ_r was the relative heading of the traffic found from Equation (5.3) and ψ_0 was the bearing to the traffic found from Equation (5.4).

$$\psi_r = \tan^{-1} \left(\frac{V_{Ax} - V_{Bx}}{V_{Ay} - V_{By}} \right) \quad (5.3)$$

$$\psi_0 = \tan^{-1} \left(\frac{Pos_{Bx} - Pos_{Ax}}{Pos_{By} - Pos_{Ay}} \right) \quad (5.4)$$

A conflict exists if $|\alpha|$ is less than β . This condition means that the relative velocity vector is inside of the conflict zone as defined by the dashed lines. If a conflict exists, a new heading for the platforms was calculated to move the relative velocity vector outside of the conflict zone. Every time-step through the simulation, this new heading was adjusted to compensate for any changes in the traffic velocity.

5.2 Resolution Heading

A resolution heading for the platforms is one that would rotate the relative velocity vector by an angle μ outside of the conflict zone. Equation (5.5) was used to calculate the needed rotation angle [29]. To find this new heading, a comparison between the speed of the platforms and the speed of the traffic was needed. If the

speed of the platforms is greater than that of the traffic, then there will be two possibilities for a resolution heading. Figure 5.2 depicts the two solutions as a counter clockwise rotation of V_A about point C to point c and a clockwise rotation of V_A about point C to point e by angles μ_c and μ_e respectively.

$$\mu = \beta - \alpha \quad (5.5)$$

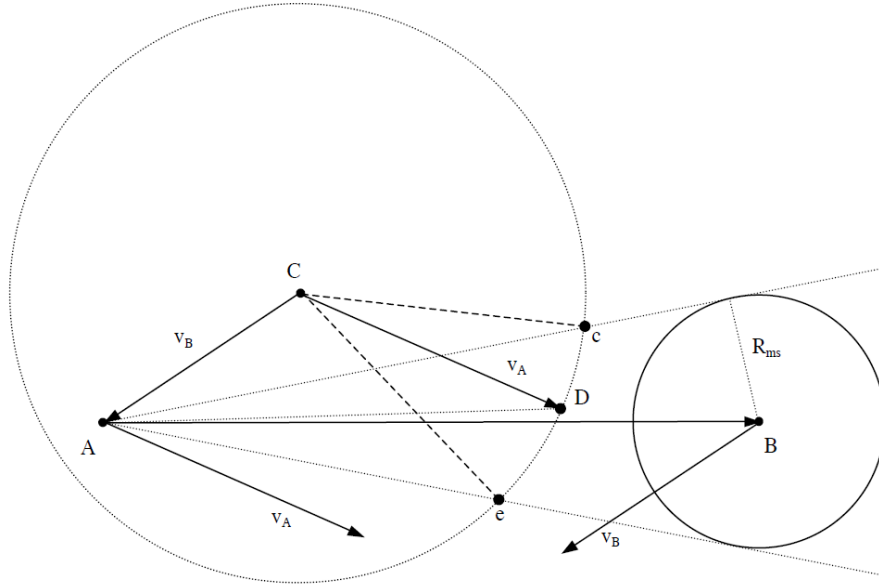


Figure 5.2: Heading Changes to Resolve Conflict ($V_A > V_B$) [29].

If the speed of the platforms is less than that of the traffic, then there will be four possibilities for a resolution heading. There will be two solutions that correspond to the upper dashed tangent line and two that correspond to the lower tangent line. Figure 5.3 depicts the four solutions as a counter clockwise rotation of V_A about point C to point c_1 or point c_2 by angles μ_{c_1} and μ_{c_2} respectively and a clockwise rotation of V_A about point C to point e_1 or point e_2 by angles μ_{e_1} and μ_{e_2} respectively.

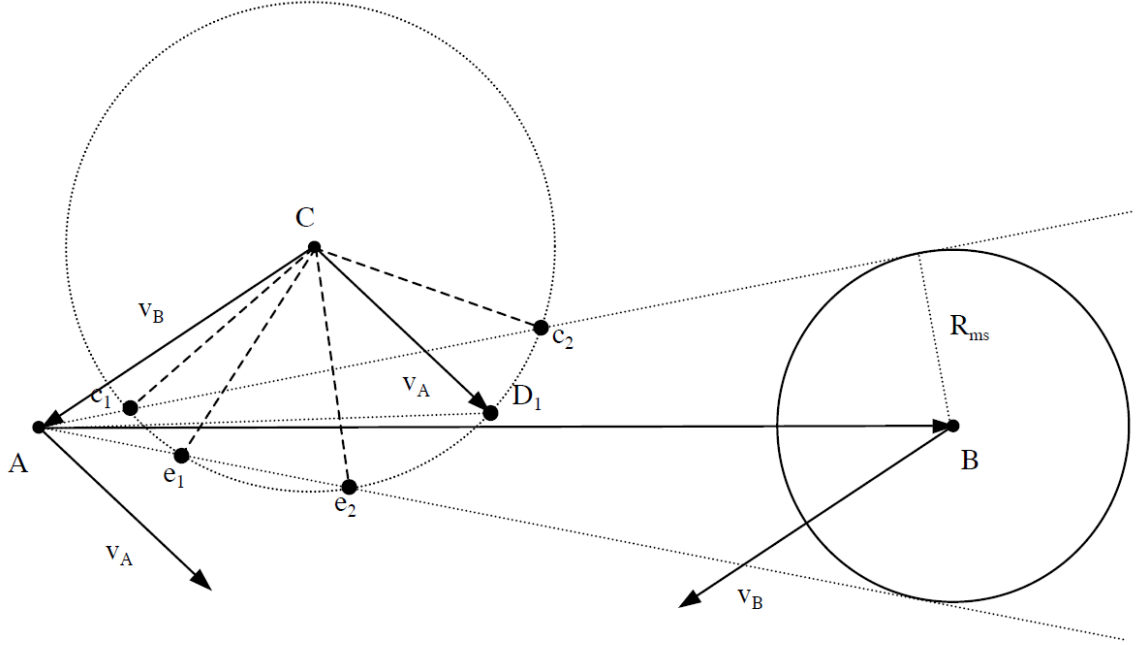
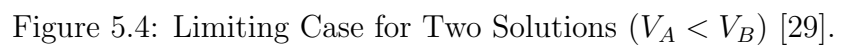


Figure 5.3: Heading Changes to Resolve Conflict ($V_A < V_B$) [29].

In the case where the speed of the platforms is less than the speed of the traffic, a limiting condition exists on the rotation angle of the relative velocity vector μ . Figure 5.4 shows the limit for two solutions to occur. Since both resolution vectors are tangent to the circle of radius $|V_A|$, trigonometry can be used to determine the maximum and minimum rotation angles that will allow two solutions to occur. Equation (5.6) describes the maximum and minimum possible rotation angles [29].

$$\begin{aligned}\mu_{max} &= \psi_B - \psi_R + \pi - \sin^{-1}\left(\frac{V_A}{V_B}\right) \\ \mu_{min} &= \psi_B - \psi_R - \pi + \sin^{-1}\left(\frac{V_A}{V_B}\right)\end{aligned}\tag{5.6}$$



Once the possible rotation angles are obtained the resolved relative heading, ψ_R^* , is calculated using Equation (5.7) for n number of possible angles.

$$\psi_R^*(n) = \psi_R + \mu(n) \quad (5.7)$$

The resolved heading for the platforms is then determined by the minimum heading change needed. The possible headings to resolve the conflict are given by Equation (5.8) for n number of possible angles [29].

$$\psi_A^*(n) = \psi_R^*(n) + \sin^{-1} \left[\left(\frac{V_B}{V_A} \right) \sin(\psi_B - \psi_R^*(n)) \right] \quad (5.8)$$

For the case when the platform speed is less than the traffic two solutions will exist for each rotation angle μ . The first solution is given by Equation (5.8) and the second is given by Equation (5.9) for each μ [29].

$$\psi_A^*(n) = \psi_R^*(n) - \sin^{-1} \left[\left(\frac{V_B}{V_A} \right) \sin(\psi_B - \psi_R^*(n)) \right] + \pi \quad (5.9)$$

Once all of the possible resolved headings were calculated, the heading that required the least amount of maneuvering was selected.

5.3 Return to Initial Flight Path

If it was determined that no traffic conflict existed and the platform UASs were both on their original flight paths, no heading change occurred. If the UASs had changed their heading to avoid a traffic conflict, but no conflict currently existed the platforms needed to maneuver themselves back to their original paths. A function was created to generate the heading needed to return to the initial flight path assuming the

measurement platforms were traveling East. Equation (5.10) determined the heading in degrees for the turn-back maneuver if the platforms maneuvered North to resolve the conflict. Equation (5.11) determined the heading in degrees for the turn-back maneuver if the platforms maneuvered South to resolve the conflict. Both equations are functions of the center position of the platforms as well as the initial heading. In the equations, $Center_{y_0}$ is the Y location in world coordinates of the center of the platform formation before the resolution maneuver and $Center_y$ is the current Y location of the formation center.

$$\psi_{TB_{mN}} = \psi_{initial} + \frac{\min(Center_y - Center_{y_0}, 2nm)}{2nm} 30^\circ \quad (5.10)$$

$$\psi_{TB_{mS}} = \psi_{initial} + \frac{\max(Center_y - Center_{y_0}, -2nm)}{2nm} 30^\circ \quad (5.11)$$

The equations above both allow for a 30° intercept angle if the platform UASs have traversed more than two nautical miles (nm) in the North or South direction to resolve the conflict. If they did not move more than two nautical miles away from their original flight path a smaller intercept angle is applied.

5.4 Resolution Heading Maneuvering

The platform heading was changed using the same PID controller as described in Section (4.7) while simultaneously changing the aop described in Section (4.1). The corrective output from the PID controller for each aircraft was the acceleration values that would maneuver the aircraft to the desired heading as well as the desired angle for measurement acquisition. The up-date rate for the platform heading controller was also 30 Hertz. Each time step, the position based off of the current velocity was

known as well as the position based off of the desired velocity. The difference between the two values was incorporated into the error in the controller.

CHAPTER 6

SYSTEM IMPLEMENTATION

To implement the SAA system described in this thesis, three main components would be needed. The first piece of hardware needed to implement the system on a UAS is optical sensors. Along with sensors, a target recognition algorithm to detect a target from a digital image is needed. Finally, to run all of the computations, an onboard computer and the wireless capability to transmit and receive data at a high rate is needed.

6.1 Optical Sensors

The sensor selection for the application should begin with the resolution requirements as well as the video capture rate. Given the size of likely threats, approximately four feet across for head-on cases, the range of three nautical miles when a target needs to be detected, and the size of the field of view described in Section (1.2), a camera with at least 1042 pixels in the horizontal plane and a capture rate of 30 frames per second is needed for this application. Equation (6.1) illustrates how the number of pixels, NoP , was determined. The recommended instantaneous field of view per pixel, $IFOVPP$, from Section (1.1) of 1.34 milliradians and a horizontal field of regard, $HFOR$, of 240° or $\frac{4}{3}\pi rad$ was used.

$$NoP = \frac{HFOR}{3} \frac{1}{IFOVPP} \quad (6.1)$$

Optical cameras such as the Creative Live Cam Notebook Ultra and the Microsoft LifeCam VX-6000 would provide adequate resolution and capture rate at a low cost. Both of these cameras have USB interfaces for connectivity to a computer.

6.2 Target Recognition

The SAA system needs a target recognition algorithm to detect a target in the digital image taken by the sensors. The algorithm must compute azimuth and elevation measurements to the target once it is detected. These measurements must be corrected for the bank and pitch angles of the measurement platform. A few examples of vision based tracking and target estimation methods accomplished by others are available in the literature [11, 12, 13, 14, 15].

6.3 Computational Processing

The SAA method described requires moderate computational power. The aircraft in the system must be able to communicate with each other as well as run the system algorithms. The computational process for the system could be handled by an onboard computer or a land based computer that communicates with the aircraft through wireless transmission. Dennis et al. employed a custom computation engine based on field-programmable gate array technology for onboard vision processing [11]. The problem with land based computers comes from the data transfer rate capabilities as well as communication range. Many UASs currently being operated are commanded from a land based computer, so there is a possibility the SAA system algorithms could be implemented on a ground station.

For onboard processing the Gumstix Verdex Pro XM4 could be used in combination with the ConsoleLCD-vx for connectivity. This processing board is equipped

with a *Marvelltm* processor and 64 megabytes of random access memory. It also has 16 megabytes of flash memory and a micro SD card adapter. To handle communications, a Maxstream XT09-SI radio modem with interface board could be used. This modem has an outdoor line of sight range capability of 40 miles and operates at a frequency of 900 megahertz.

6.4 Weight Analysis

Weight considerations need to be made when deciding on the sensors to incorporate as well as the computational processing method chosen to increase the payload capability of the UAS the system is implemented on. Large onboard computers add significant weight to the SAA system total. The Helios board used in the onboard system mentioned above only weighs 36 grams or approximately 1.3 ounces. Both of the camera types mentioned as possible optical sensors weigh approximately 3.2 ounces each. Table 6.1 is a list of needed hardware and the component weights as well as the size and power required for each. Table 6.2 is a list of the total weight and total power required for the system.

Item	Size LxWxH (in.)	Power (w)	Weight (oz)
Camera	3 x 2.2	4.8	3.2
Image Processor	2.56 x 3.56 x 0.75	0.16	1.3
Processing Board	1.31 x 3.13 x 0.44	1.5	0.8
Radio Modem	4 x 2.5 x 0.75	3.5	0.64
Radio Antenna	6.5 x 0.38	-	5.2

Table 6.1: Hardware Component Specifications.

Item	Quantity	Total Power (w)	Total Weight (oz)
Camera	3	14.4	9.6
Image Processor	3	0.48	3.9
Processing Board	1	1.5	0.8
Radio Modem	1	3.5	0.64
Radio Antenna	1	-	5.2
Total		19.88	20.14

Table 6.2: Total System Weight and Power Required.

CHAPTER 7

RESULTS

Each of the twelve simulation cases presented were run on Dell Optiplex 755 machines equipped with Intel Core 2 Duo processors operating at 2.2 gigahertz with two gigabytes of random access memory. Monte Carlo simulations consisting of 1000 iterations were used for each scenario that simulated six minutes in time. Monte Carlo simulations were used to account for the random measurement noise associated with the measurement model. System comparisons were made with and without conflict resolution to show the advantages of the optimal measurement controller. Two main alternative systems were generated to determine differences in the range estimate, the distance with which the platforms avoided the traffic, in the case when the conflict resolution controller was activated, and the total distance traveled by each UAS in the system. In the comparison simulations for each system the filter was initialized based on the true range to the target. The effect of platform separation distance was also determined by varying the measurement platform spacing in two simulations by ± 500 feet. Also, the UAS performance parameters of specific excess power and maximum rate of turn were varied to determine their effect on the conflict resolution controller and the range estimate. For all of the varying parameter simulations, the filter was initialized based on the initial measurements. Lastly, two simulations were run with varying target scenarios to determine the reliability of the system. Table 7.1 lists the specific parameters for each simulation.

Simulation #	Formation Description	Conflict Resolution Capability	Separation Distance (ft)	Maximum Rate of Turn (deg/min)	Specific Excess Power
1	Optimal Measurement Maneuvering	Inactive	1000	180	1000
2	3 Platforms, Fixed Orientation	Inactive	1000	180	1000
3	Platforms Orbiting Formation Center	Inactive	1000	180	1000
4	Optimal Measurement Maneuvering	Active	1000	180	1000
5	3 Platforms, Fixed Orientation	Active	1000	180	1000
6	Platforms Orbiting Formation Center	Active	1000	180	1000
7	Optimal Measurement Maneuvering	Active	500	180	1000
8	Optimal Measurement Maneuvering	Active	1500	180	1000
9	Optimal Measurement Maneuvering	Active	1000	90	500
10	Optimal Measurement Maneuvering	Active	1000	270	1500
11	Optimal Measurement Maneuvering	Active	1000	180	1000
12	Optimal Measurement Maneuvering	Active	1000	180	1000

Table 7.1: Specific Simulation Parameters.

7.1 Alternative Systems

The first alternative considered was of three measurement platforms flying in a fixed formation. Three platforms were used in order to ensure at least two platforms would be able to take measurements on the traffic at all convergence angles. Measurements from two platforms are needed so that some sort of range information can be deduced. Figure 7.1 illustrates the three platform formation.

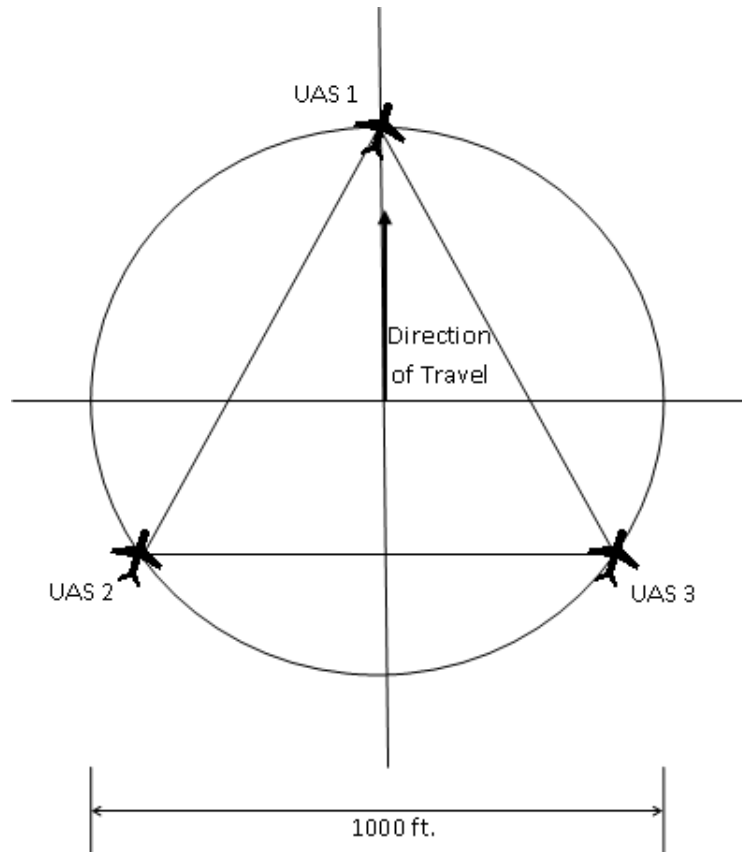


Figure 7.1: Three Platform Formation.

The second alternative considered was of two measurement platforms flying in a formation that rotated constantly about its center at an angular velocity of 90 deg/min. Rotating constantly allowed the two UASs to gather range information on

traffic at all convergence angles at various time intervals. Figure 7.2 illustrates the constantly rotating two platform formation.

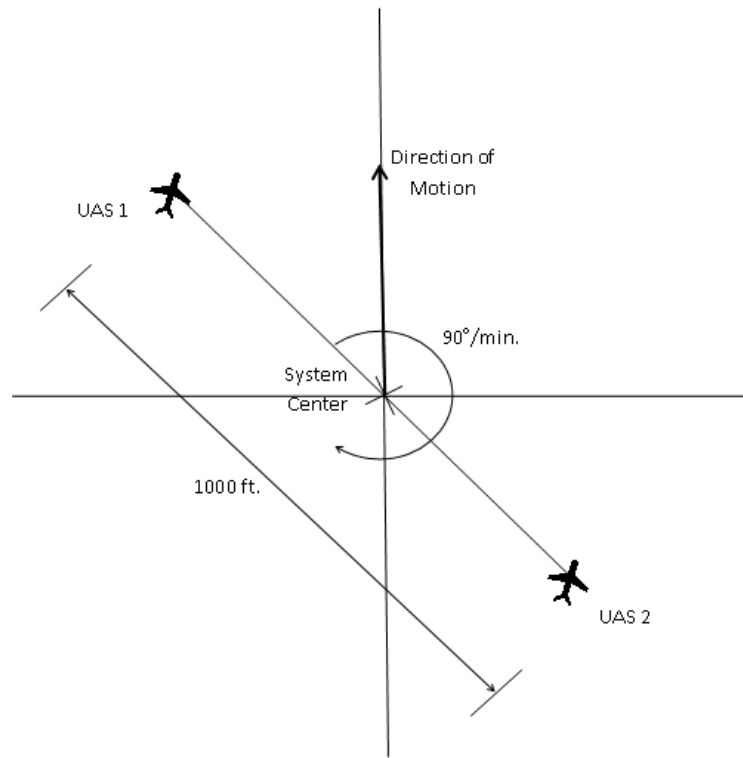


Figure 7.2: Constantly Rotating Two Platform Formation.

7.2 Comparison Target Scenario

To keep the comparison between systems equivalent, the same number of targets and the same target flight tracks were used for each scenario simulated. Figure 7.3 illustrates a top view of the scenario. Similar to several figures in the remainder of the chapter, the platforms are depicted in blue and the traffic is in red. The platforms had a heading of 090° and a speed of 100 knots. Air traffic approached the flight path of the platforms at various angles. The first target started 500 feet East of the platforms and five miles North at a speed of 140 knots with a heading of 135° . The second target originated 10 miles East of the platforms and 12 miles North at a speed

of 145 knots with a heading of 225° . The third target originated 17 miles East of the platforms and nine miles South at a speed of 120 knots with a heading of 315° . The final target originated 500 feet West of the platforms and seven miles South at a speed of 145 knots with a heading of 045° .

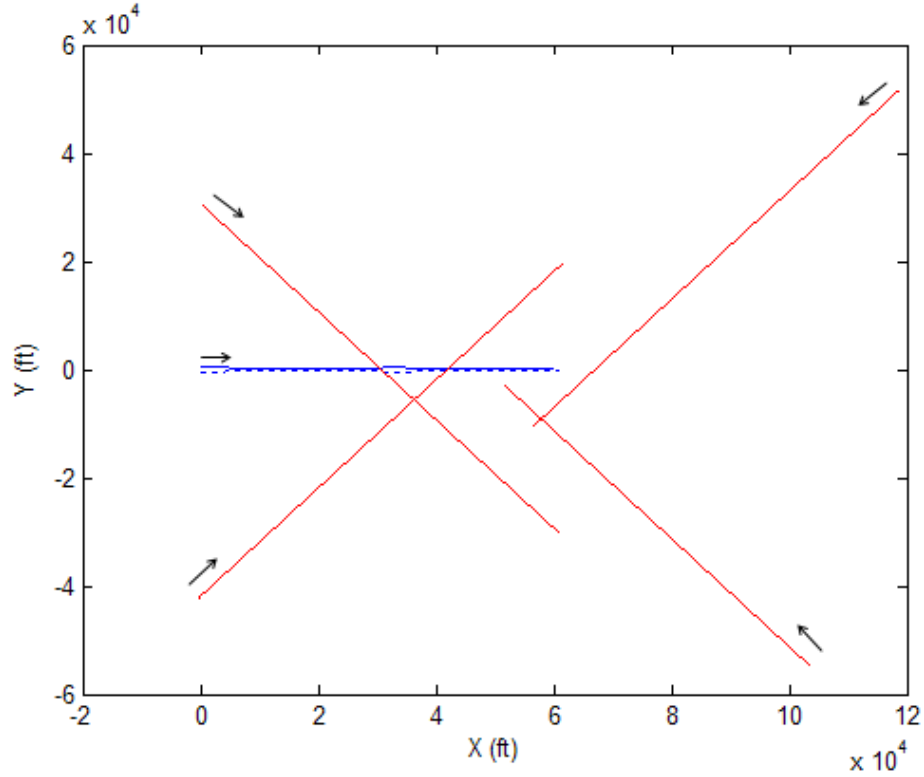


Figure 7.3: Comparison Scenario; Y-Axis Points North.

7.3 Comparison Without Conflict Resolution

A comparison was made between the three formation types without conflict resolution to determine the penalty for maneuvering to take optimal measurements. The average percent error in the estimated range was calculated after all of the Monte Carlo iterations. The average percent difference in excess distance traveled was also computed for each of the cases. For each of the systems, the error starts at zero

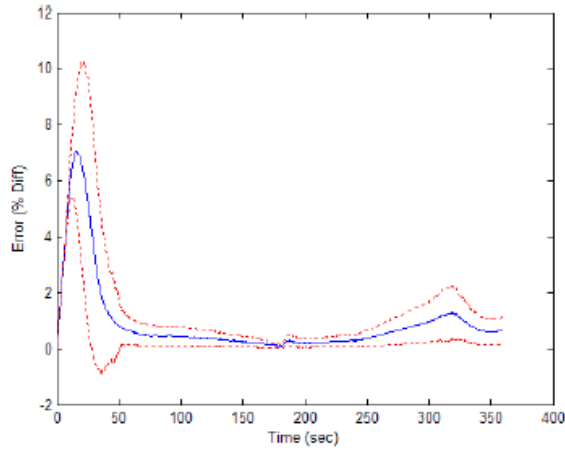
because it is initialized with the true range. The velocity however, is initialized to zero so the range error grows until the filter is able to estimate velocity accurately.

7.3.1 Range Error

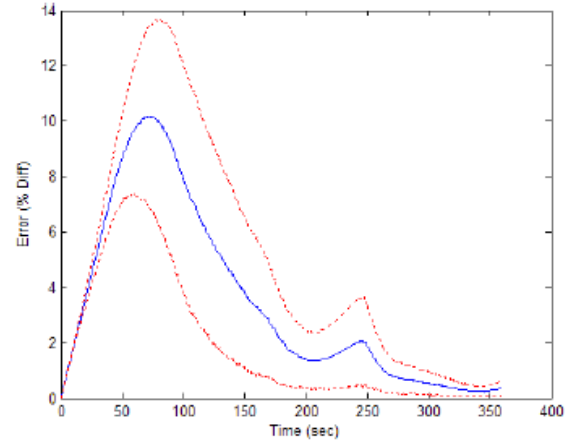
For the system with two measurement platforms maneuvering to take optimal measurements, Figure 7.4 depicts the averages and standard deviations of the estimated range error for each of the four targets after 1000 Monte Carlo iterations. The maximum average error for targets one and four occurred within the first few seconds of simulation. Targets one and four were the two targets that the controller was maneuvering toward to take optimal measurements. After the first spike in error for both of these targets, the range estimate error decreased rapidly. The location of minimum range error for targets one and four reveal the time of closest approach for each of the respective targets.

For the system with three measurement platforms flying in a fixed formation to take measurements, Figure 7.5 depicts the averages and standard deviations of the estimated range error for each of the four targets. The maximum average error for target one again occurred during filter initialization. The maximum error for target four resembled that from target one. This was due to the formation being symmetrical and the two target tracks closely resembling each other at different headings. Again, the location of minimum range error for targets one and four reveal the time of closest approach for each of the respective targets.

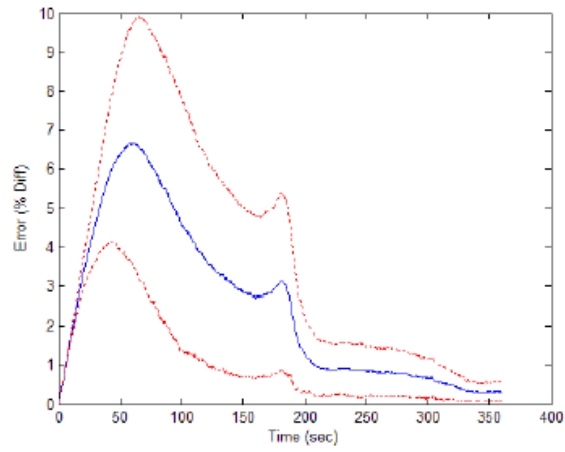
For the system with two measurement platforms constantly orbiting the center of their formation to take optimal measurements, Figure 7.6 depicts the averages of the estimated range error for each of the targets. For each of the targets the oscillation in the range estimate from the orbiting platforms was exhibited. The error then gradually decreased throughout the simulation. The range error plots of target one



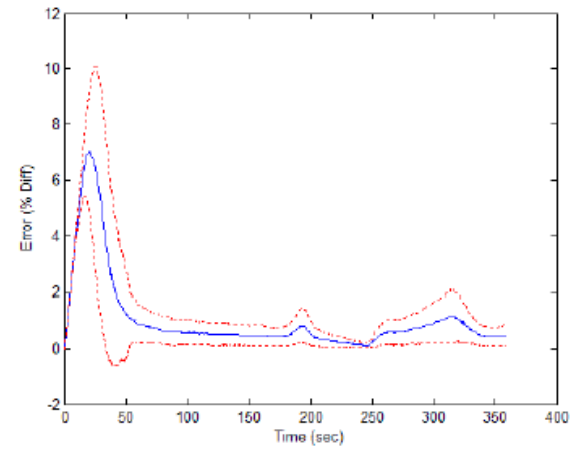
(a) Target 1.



(b) Target 2.

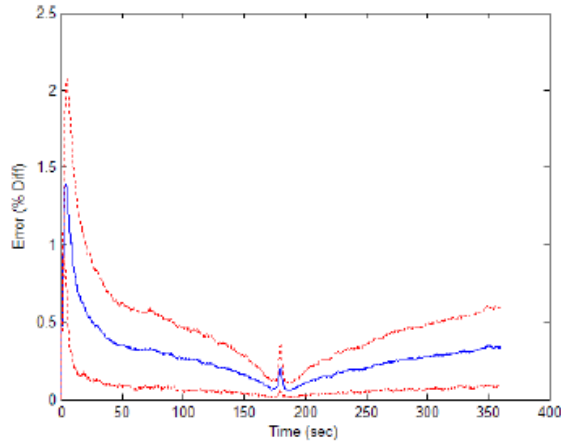


(c) Target 3.

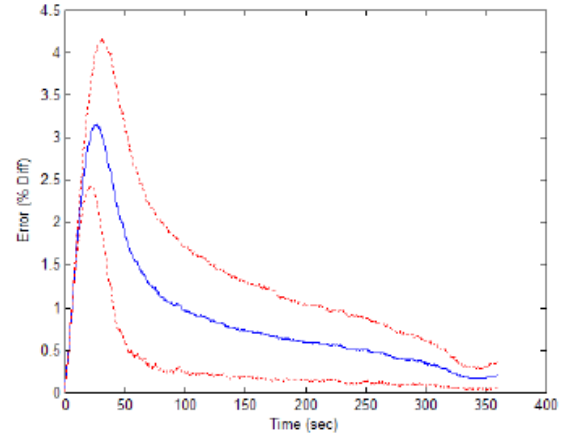


(d) Target 4.

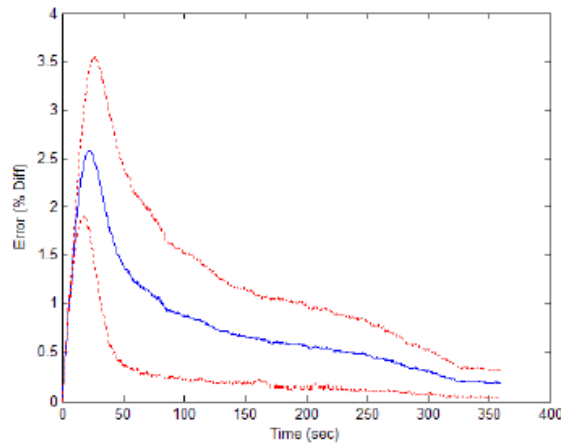
Figure 7.4: Average Range Error (Blue Line) and Standard Deviation (Red Line) for System 1.



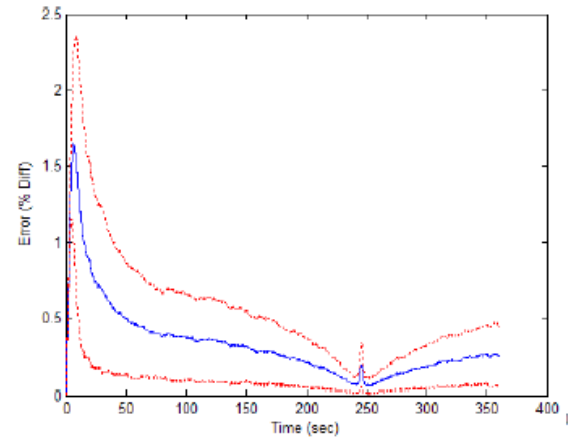
(a) Target 1.



(b) Target 2.



(c) Target 3.



(d) Target 4.

Figure 7.5: Average Range Error (Blue Line) and Standard Deviation (Red Line) for System 2.

and four again reveal the time of closest approach of 180 and 250 seconds respectively.

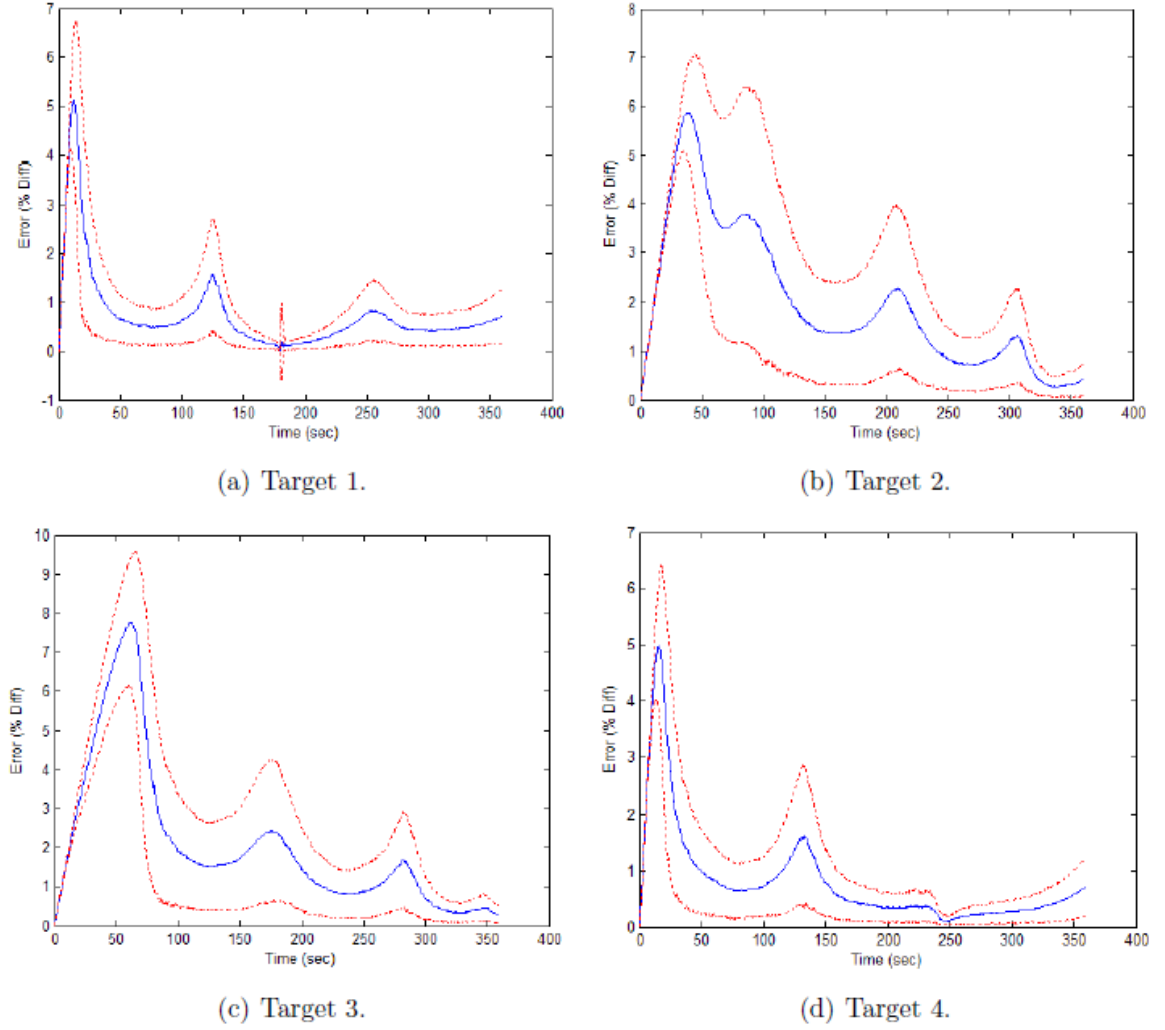


Figure 7.6: Average Range Error (Blue Line) and Standard Deviation (Red Line) for System 3.

Table 7.2 summarizes the range error comparison without conflict resolution. The optimal maneuvering formation and the orbiting formation had comparable estimates for each of the targets.

The range error plots for the first two cases, optimal measurement maneuvering and three platforms, are similar after the filter is initialized and the platforms

Formation Description	Target	Maximum Error (%)	Time of Maximum Error (sec)	Minimum Error (%)	Time of Minimum Error (sec)
Optimal Measurement Maneuvering	1	7	20	0.25	175
	2	10	85	0.2	340
	3	6.5	60	0.4	350
	4	7	25	0.4	250
3 Platforms, Fixed Orientation	1	1.5	5	0.08	180
	2	3	40	0.25	340
	3	2.5	35	0.25	360
	4	1.7	15	0.08	250
Platforms Orbiting Formation Center	1	5	20	0.2	180
	2	6	45	0.4	340
	3	8	60	0.3	360
	4	5	20	0.19	250

Table 7.2: Summary of Range Error Plots without Conflict Resolution.

maneuver to obtain the best measurements. The only difference in range error for these two cases comes from the maximum error. With the three platform case there is no convergence angle in the FOR to prevent the platforms from obtaining range information. Therefore, as soon as a target is detected accurate range information can be obtained. With the optimal maneuvering case however, there is a time lag between when the target is detected and when accurate range information can be deduced. This time lag comes from the maneuvering time for the UASs to reposition themselves. For each of the targets, it was during this maneuvering time that the error peaked. Once repositioned, the range estimates decreased.

With the orbiting formation, the range error throughout the simulation varies greatly. Since the orbiting platforms are unable to obtain optimal measurements for more than a short period of time, an oscillation in the range error occurs. As the platforms orbit into a position to take optimal measurements, the range error becomes less. As they orbit away from this position, the range error grows. This happens with each half orbit of the platforms. The overall divergence in the range error for the

orbiting case comes from the time history of measurements and position estimates from the EKF.

Figure 7.7 depicts the averages of the estimated range error for each of the targets. The differences from system one, the optimal maneuvering formation, from the other systems comes from the initial filter estimate in each of the simulations. For target one, the time range of concern is from 75 to 175 seconds. For target two, the time of concern is between 175 and 325 seconds. For targets three and four the time of concern is between 225 and 360 seconds.

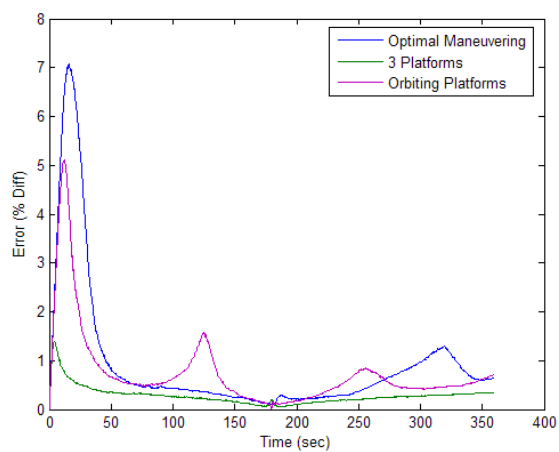
7.3.2 Excess Distance Traveled

For the system with two measurement platforms maneuvering to take optimal measurements, Table 7.3 summarizes the average percent difference in distance traveled for both measurement platforms as well as the corresponding standard deviations.

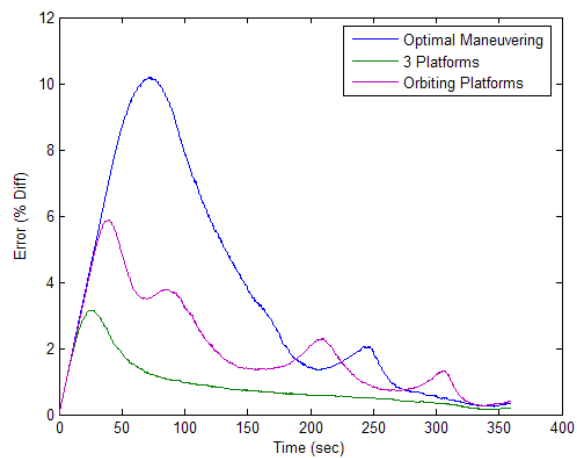
UAS	Excess Distance (% Difference)	Standard Deviation (%)
Platform 1	0.204	0.0277
Platform 2	0.184	0.0256

Table 7.3: Average Excess Distance Traveled and Standard Deviation for System 1.

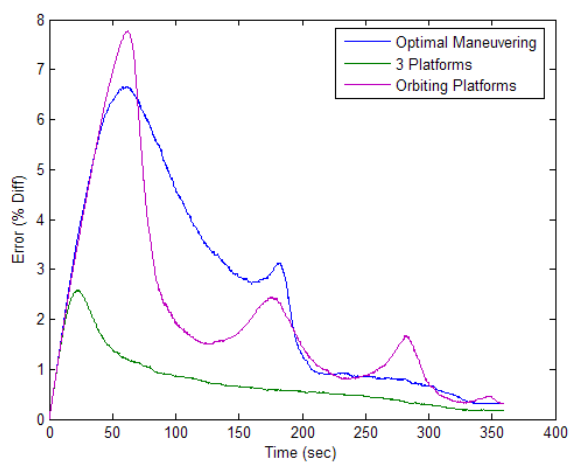
For the system with three measurement platforms flying in a fixed formation to take measurements, the average percent difference in distance traveled for all three measurement platforms as well as the corresponding standard deviations was zero. This is because with this system the UASs only travel from their initial position to their final position. Since the formation contains three aircraft, the UASs do not have to maneuver to take measurements.



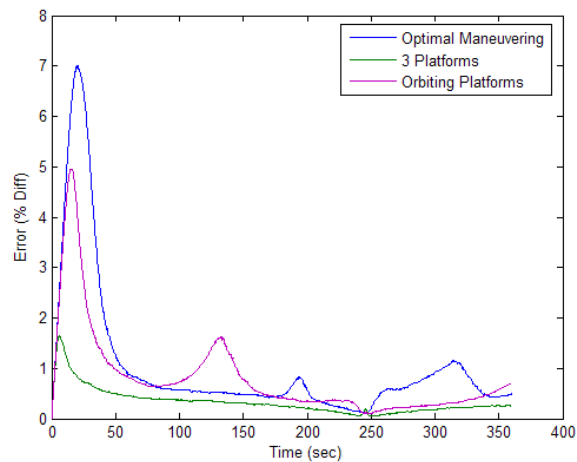
(a) Target 1.



(b) Target 2.



(c) Target 3.



(d) Target 4.

Figure 7.7: Average Range Error Comparison.

For the system with two measurement platforms constantly orbiting the center of their formation to take optimal measurements, Table 7.4 summarizes the average percent difference in distance traveled for both measurement platforms as well as the corresponding standard deviations. On average, platform one traveled 0.24% farther than the straight line distance between its initial and final positions. Platform two traveled an average of 0.25% farther.

UAS	Excess Distance (% Difference)	Standard Deviation (%)
Platform 1	0.242	1.44E-15
Platform 2	0.251	1.83E-15

Table 7.4: Average Excess Distance Traveled and Standard Deviation for System 3.

After examining the excess-distance data from the comparison without conflict resolution it was determined that the penalty for maneuvering to take optimal measurements was minuscule. The excess distance traveled was around 0.2%. The excess distance incurred when the platforms constantly orbit the center of the formation was slightly higher at around 0.25%. While the three platform formation had no excess distance, the required use of another aircraft eliminates any gain from a decrease in excess distance. It could be argued that the excess distance for this formation was actually the entire distance traveled by the third aircraft.

7.4 Conflict Resolution Algorithm Verification

Before a comparison was made using conflict resolution, the resolution heading algorithm was verified. This was done by running the optimal measurement maneuvering formation in 16 different simulations. For each simulation, the collision point was set to occur three nautical miles from the platform starting location. For the

first eight simulations, the target speed was held constant at 75 knots and the target heading was varied from 0 to 315° by 45° increments. The target speed was set to 75 knots to verify the part of the conflict resolution algorithm used when the conflicting traffic is traveling slower than the platforms. Figure 7.8 and Figure 7.9 show the top view of each target scenario. The conflicting traffic is depicted in red and the measurement platforms are blue. The green in each image is the area of uncertainty.

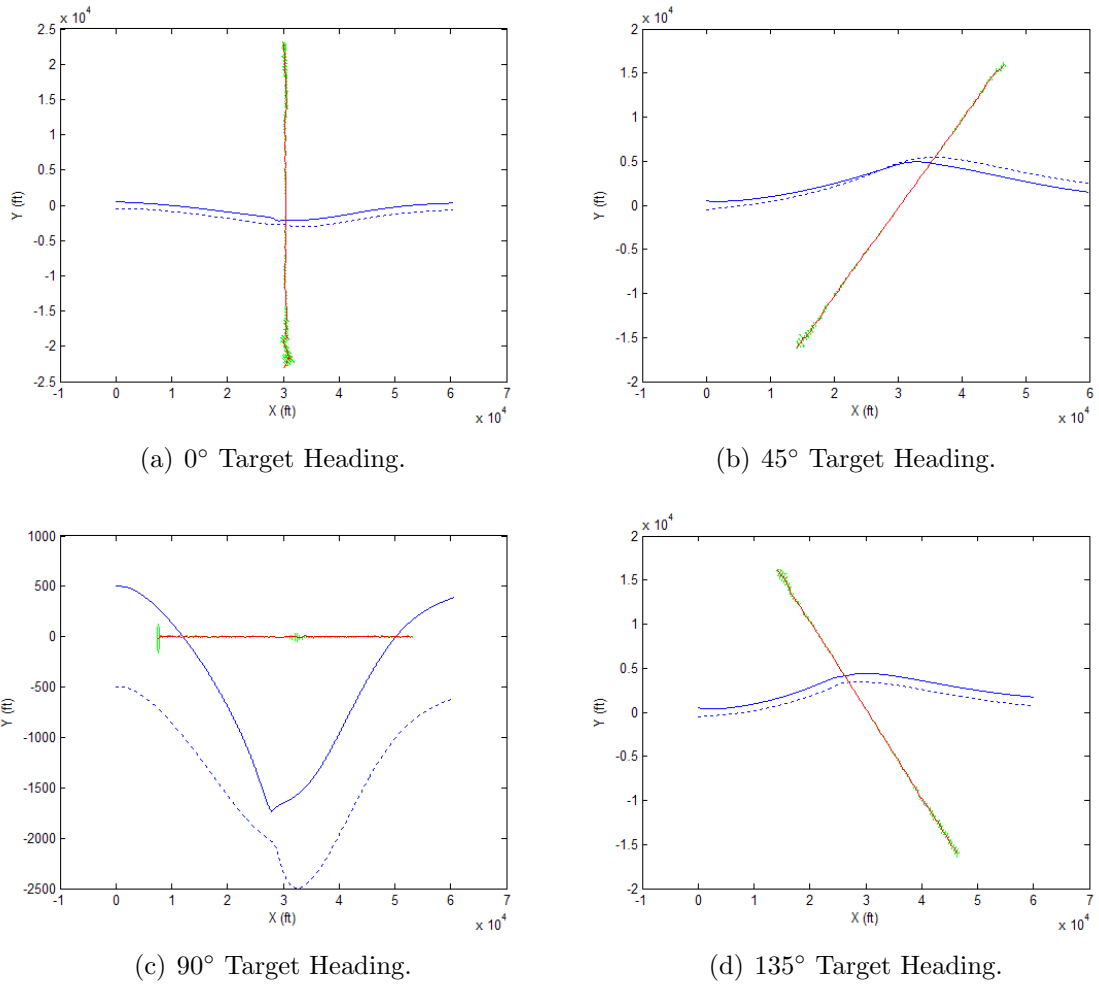
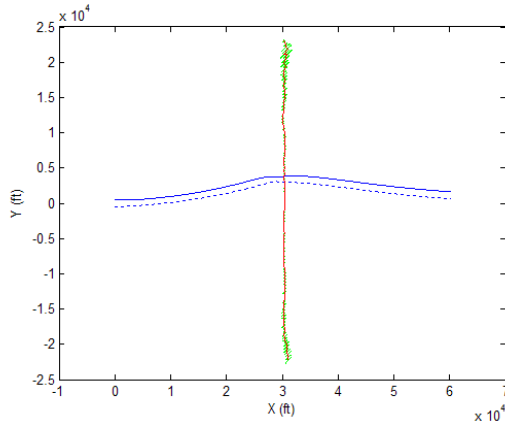
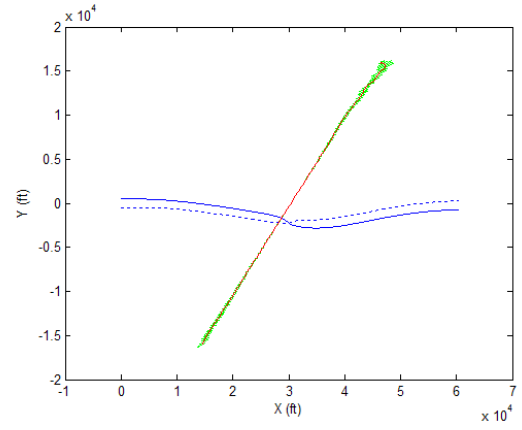


Figure 7.8: First Four Verification Target Positions Traveling at 75 knots.

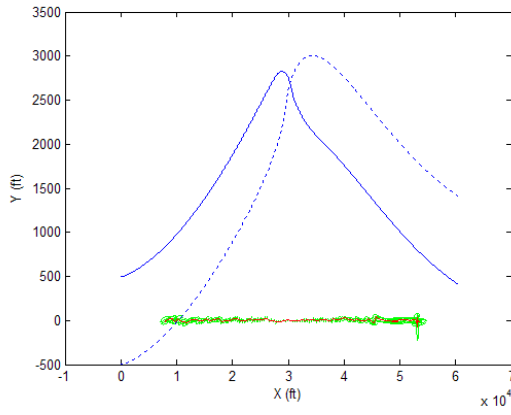
For the last eight simulations, the target speed was held constant at 125 knots and the target heading was again varied from 0 to 315° by 45° increments. The faster



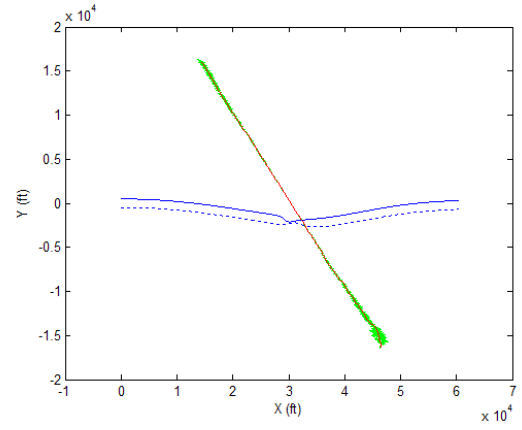
(a) 180° Target Heading.



(b) 225° Target Heading.



(c) 270° Target Heading.



(d) 315° Target Heading.

Figure 7.9: Last Four Verification Target Positions Traveling at 75 knots.

target speed was used to verify the second part of the conflict resolution algorithm used when the conflicting traffic is traveling faster than the platforms. Figure 7.10 and Figure 7.11 show the top view of each target scenario. The conflicting traffic is depicted in red and the measurement platforms are blue.

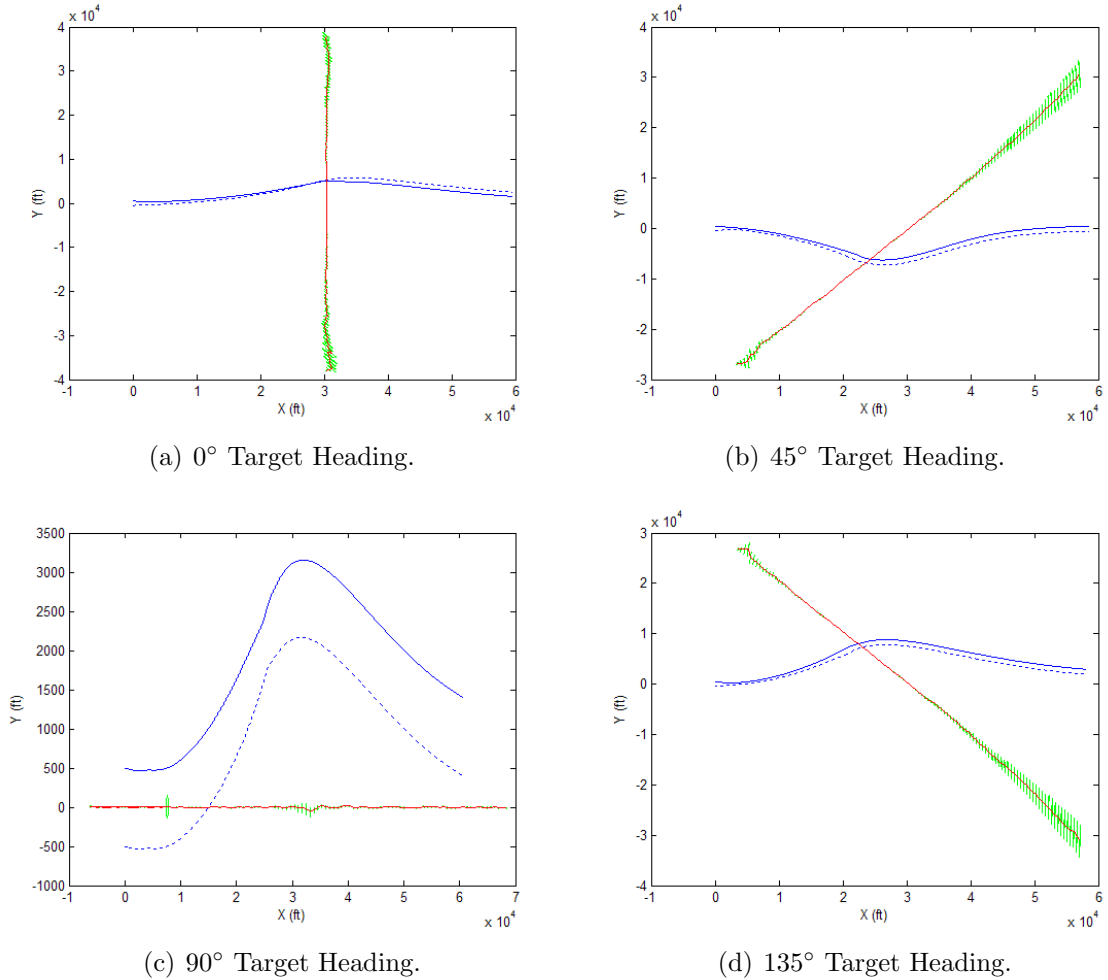
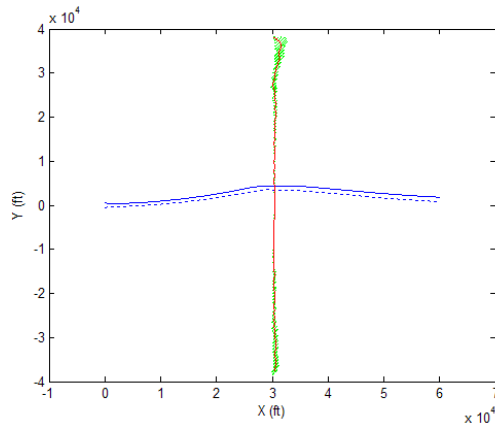
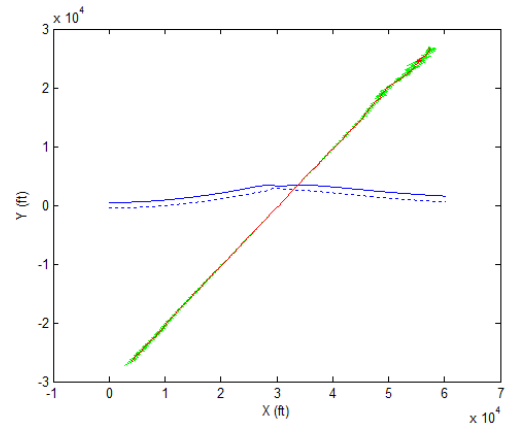


Figure 7.10: First Four Verification Target Positions Traveling at 125 knots.

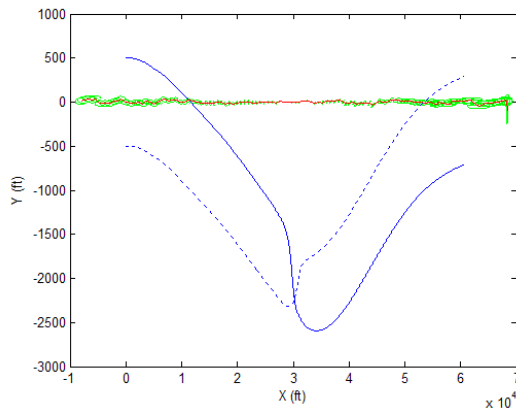
Table 7.5 summarizes the miss distances for each target scenario shown above. Since all of the miss distances were near the specified distance of 2000 feet, it was concluded the conflict resolution algorithm was working properly.



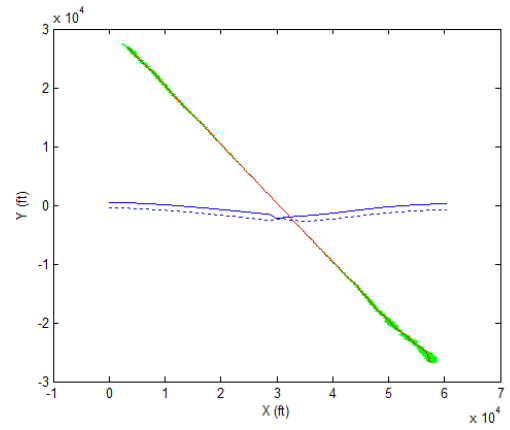
(a) 180° Target Heading.



(b) 225° Target Heading.



(c) 270° Target Heading.



(d) 315° Target Heading.

Figure 7.11: Last Four Verification Target Positions Traveling at 125 knots.

Speed	75 knots	125 knots
Traffic Heading (deg.)	Miss Distance (ft.)	Miss Distance (ft.)
0	1996	2885
45	2956	1915
90	1995	2568
135	2695	1942
180	2820	2617
225	1995	2822
270	2552	2010
315	1997	1997

Table 7.5: Miss Distances for Verification Targets.

7.5 Comparison With Conflict Resolution

A comparison was made between the three systems with conflict resolution to determine how the proposed method of maneuvering to take optimal measurements performs. The average percent error in the estimated range was calculated after all of the Monte Carlo simulations. The average miss distance, the distance with which the platforms avoided the traffic, was also calculated along with the standard deviation. The miss distance was measured from the formation center. In order to prevent a near midair collision, the miss distance must be greater than half of the separation distance plus 500 feet. For the proposed system, this means the miss distance must be greater than 1000 feet. To compensate for measurement noise and to ensure a near miss did not occur, the minimum miss distance used by the conflict resolution algorithm was set to 2000 feet for each of the simulations. The average percent difference of excess distance traveled was also computed for each of the cases.

7.5.1 Range Error

For the system with two measurement platforms maneuvering to take optimal measurements, Figure 7.12 depicts the averages and standard deviations of the estimated range error for each of the four targets. The maximum average error for targets one and four again occurred within the first few seconds of the simulation while the filter was unable to accurately estimate the target velocity. After the first minute of simulation, the error in the range estimate for targets one and four, the closer of the four targets, decreased.

For the system with three measurement platforms flying in a fixed formation to take measurements, Figure 7.13 depicts the averages of the estimated range error for each target. The relation in error for targets one and four is again due to the formation being symmetrical and the two target tracks closely resembling each other at different headings. After the first spike in error for targets two and three, the range estimates gradually decreased as time progressed in the simulation.

For the system with two measurement platforms constantly orbiting the center of their formation to take optimal measurements, Figure 7.14 depicts the averages of the estimated range error for each target. The error for target one has two other peaks aside from the maximum value. This is from the platforms orbiting and the quality of the measurements changing with time. The average error for target two gradually decreased as the time history going into the filter increased. With each of the targets, the oscillating measurement quality due to the orbiting of the platforms is exhibited.

Table 7.6 summarizes the range error comparison with conflict resolution. Both the optimal maneuvering and orbiting formations had similar minimum estimated range error for targets one and four.

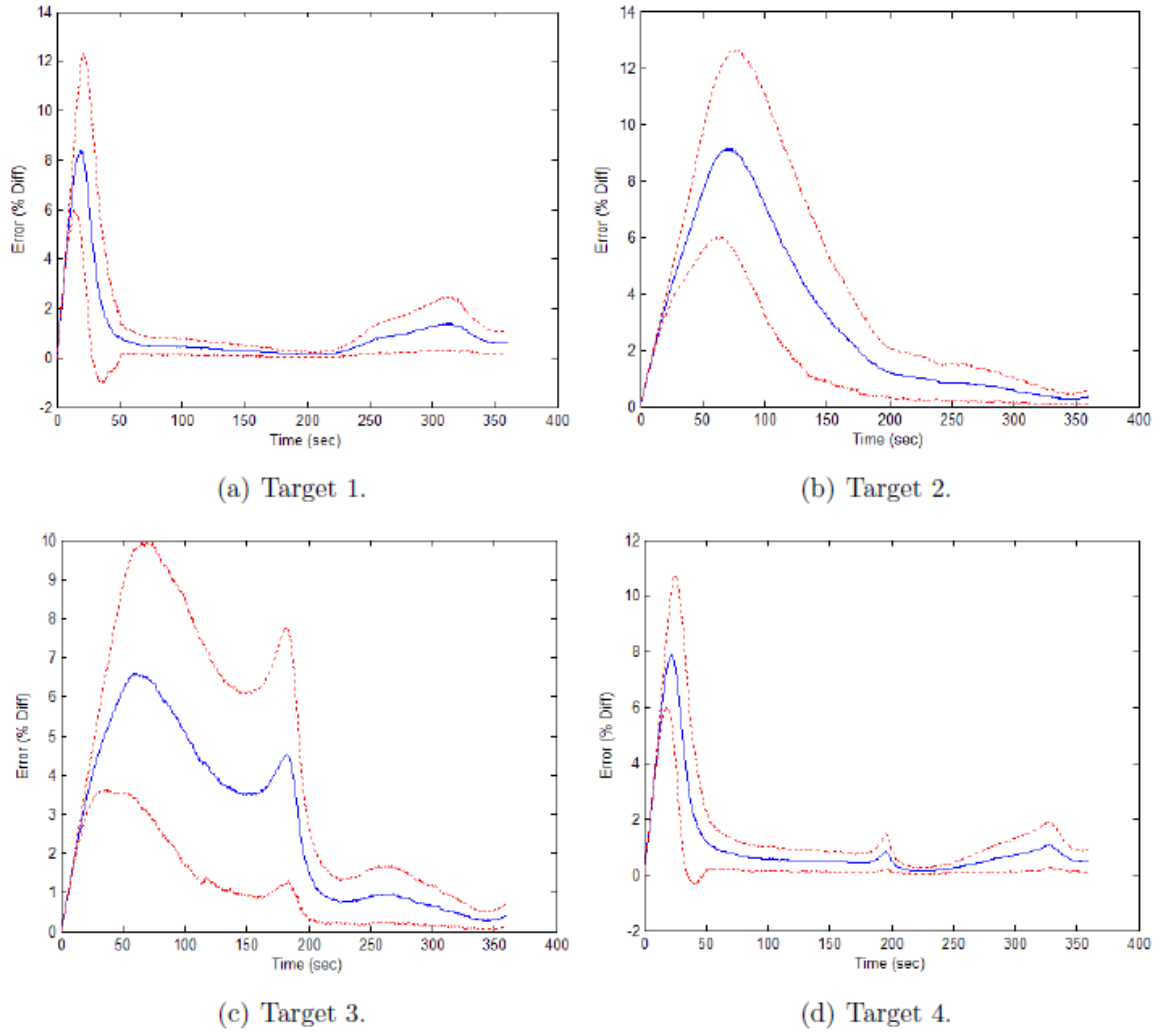
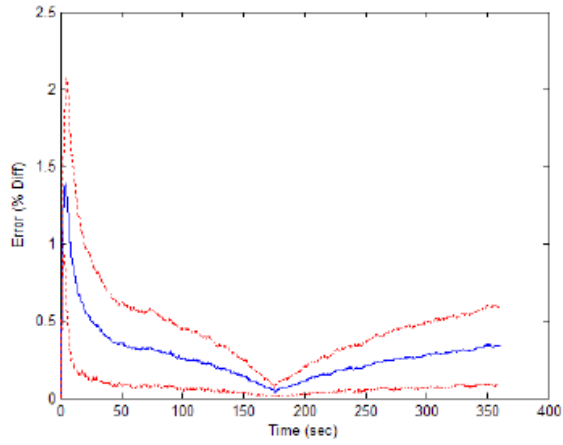
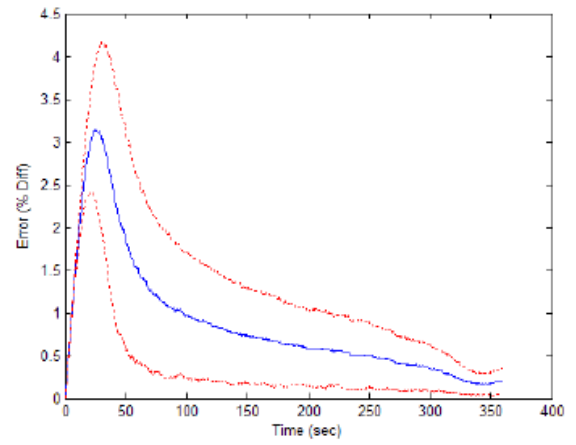


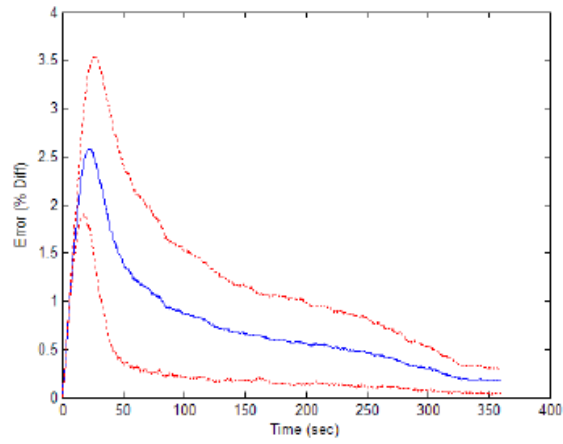
Figure 7.12: Average Range Error (Blue Line) and Standard Deviation (Red Line) with Conflict Resolution for System 1.



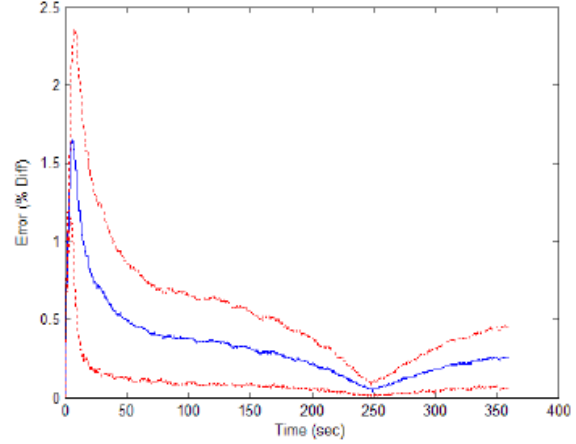
(a) Target 1.



(b) Target 2.

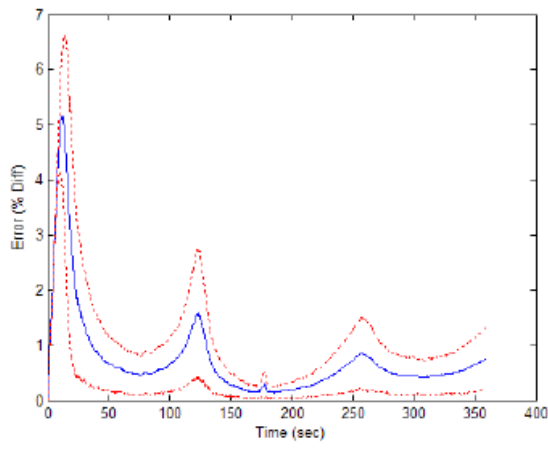


(c) Target 3.

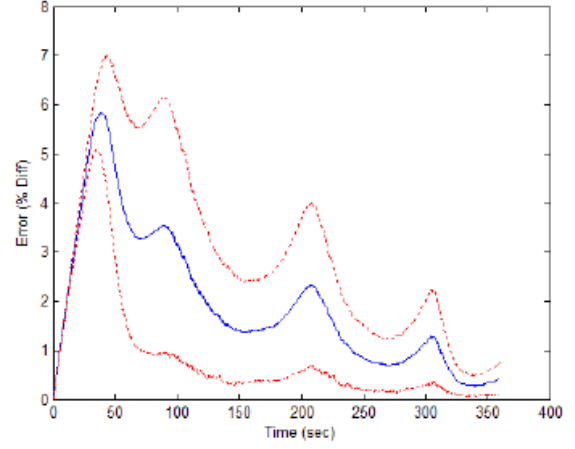


(d) Target 4.

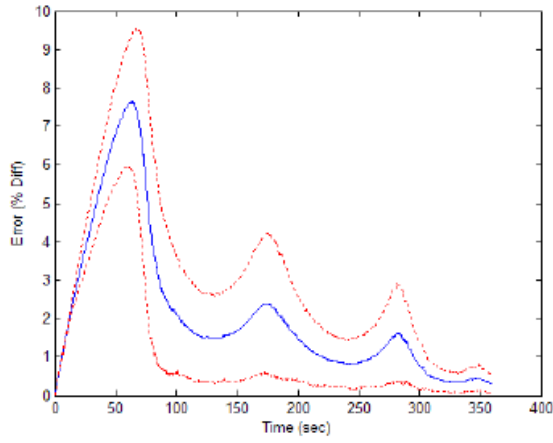
Figure 7.13: Average Range Error (Blue Line) and Standard Deviation (Red Line) with Conflict Resolution for System 2.



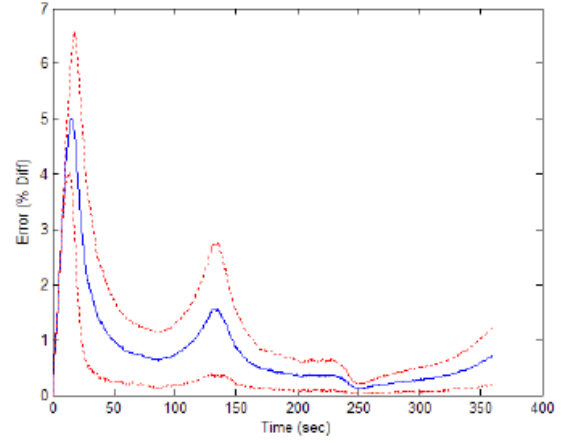
(a) Target 1.



(b) Target 2.



(c) Target 3.



(d) Target 4.

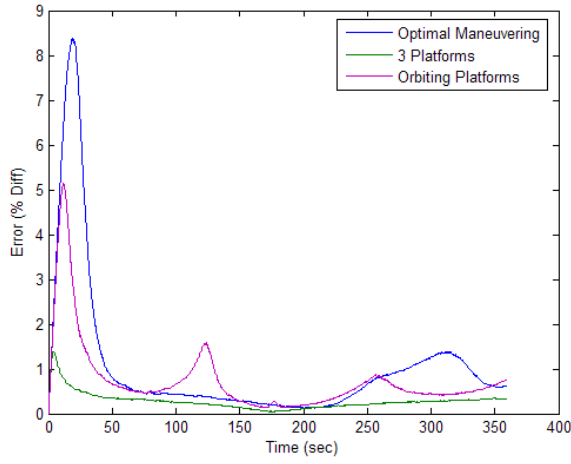
Figure 7.14: Average Range Error (Blue Line) and Standard Deviation (Red Line) with Conflict Resolution for System 3.

Formation Description	Target	Maximum Error (%)	Time of Maximum Error (sec)	Minimum Error (%)	Time of Minimum Error (sec)
Optimal Measurement Maneuvering	1	8	20	0.3	190
	2	9	85	0.25	340
	3	6.5	65	0.4	340
	4	8	25	0.35	220
3 Platforms, Fixed Orientation	1	1.35	2	0.05	180
	2	3.2	40	0.25	345
	3	2.6	20	0.25	360
	4	1.7	10	0.08	250
Platforms Orbiting Formation Center	1	5.1	15	0.2	180
	2	5.9	48	0.4	330
	3	7.5	65	0.3	360
	4	5	25	0.18	250

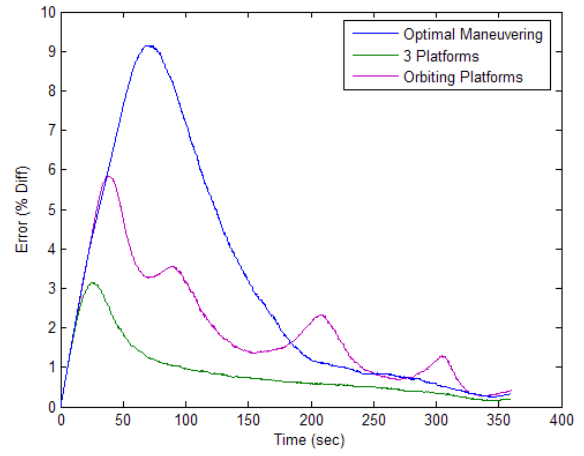
Table 7.6: Summary of Range Error Plots with Conflict Resolution.

The range error plots for each of the comparison formation types with conflict resolution capability look similar to the range error plots obtained when the formations did not possess the ability to resolve traffic conflicts. This suggests the conflict resolution controller does not affect the ability to obtain an accurate range estimate. The three platform formation still provided a better range estimate initially, but, given the time to maneuver, the optimal maneuvering formation produced range error values that closely compared for targets one and four. The increased error for the orbiting formation again suggests that this formation is not the optimal solution.

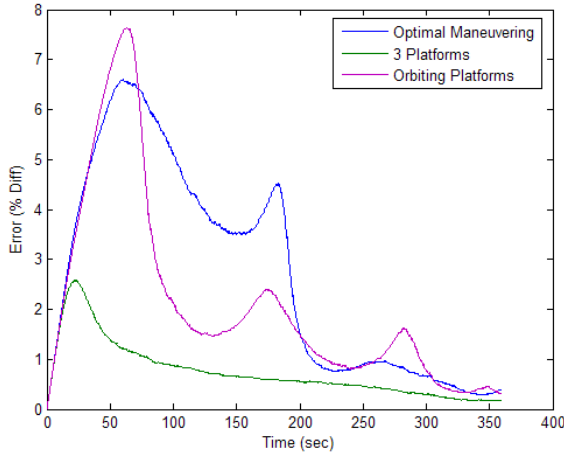
Figure 7.15 depicts the averages of the estimated range error for each of the targets. The differences from system one, the optimal maneuvering formation, from the three platform formation again comes from the better initial filter estimate in each of the simulations. For target one, the time range of concern is from 75 to 175 seconds. For target two, the time of concern is between 175 and 325 seconds. For targets three and four the time of concern is between 225 and 360 seconds.



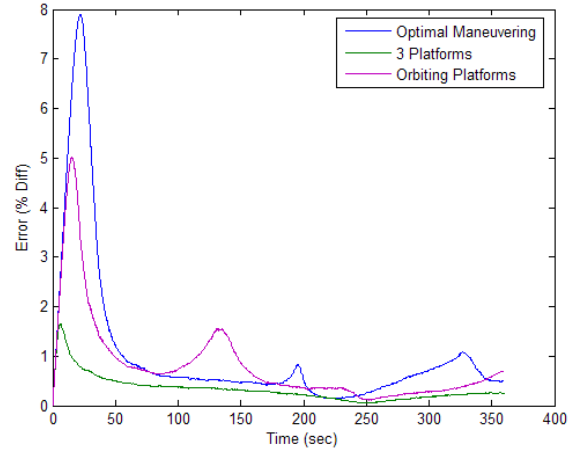
(a) Target 1.



(b) Target 2.



(c) Target 3.



(d) Target 4.

Figure 7.15: Average Range Error Comparison with Conflict Resolution.

7.5.2 Excess Distance Traveled and Miss Distance

For the system with two measurement platforms maneuvering to take optimal measurements, Table 7.7 summarizes the average percent difference in distance traveled for both measurement platforms as well as the corresponding standard deviations. Table 7.8 lists the average miss distance for each target along with the corresponding standard deviations. On average, platform one traveled 1.5% farther than the straight line distance between its initial and final positions. Platform two traveled an average of 1.09% farther. Approximately $\frac{4}{5}$ of the excess distance traveled was from the conflict resolution.

UAS	Excess Distance (% Difference)	Standard Deviation (%)
Platform 1	1.49	1.4
Platform 2	1.090	1.5

Table 7.7: Average Excess Distance Traveled and Standard Deviation for System 1 with Conflict Resolution.

Traffic	Average Miss Distance (ft.)	Standard Deviation (ft.)	Minimum Miss Distance (ft.)
Target 1	1799	39.9	1759
Target 2	7905	53.9	7851
Target 3	5340	59.0	5281
Target 4	2088	33.1	2055

Table 7.8: Average and Minimum Miss Distances and Standard Deviations for System 1 with Conflict Resolution.

For the system with three measurement platforms flying in a fixed formation to take measurements, the average percent difference in distance traveled for all three measurement platforms was 0.258%. This is because with this system the UASs travel in the same formation throughout the flight. The excess distance only comes from

the conflict resolution maneuver. Table 7.9 lists the average miss distance for each target along with the corresponding standard deviations.

Traffic	Average Miss Distance (ft.)	Standard Deviation (ft.)	Minimum Miss Distance (ft.)
Target 1	1798	39.9	1758
Target 2	7963	53.9	7909
Target 3	5284	59.0	5225
Target 4	2108	33.1	2075

Table 7.9: Average and Minimum Miss Distances and Standard Deviations for System 2 with Conflict Resolution.

For the system with two measurement platforms constantly orbiting the center of their formation to take optimal measurements, Table 7.10 lists the average percent difference in distance traveled for both measurement platforms as well as the corresponding standard deviations. Table 7.11 lists the average miss distance for each target along with the corresponding standard deviations. On average, platform one traveled 1.8% farther than the straight line distance between its initial and final positions. Platform two traveled an average of 1.6% farther.

UAS	Excess Distance (% Difference)	Standard Deviation (%)
Platform 1	1.762	0.248
Platform 2	1.634	0.250

Table 7.10: Average Excess Distance Traveled and Standard Deviation for System 3 with Conflict Resolution.

When the excess distances traveled were compared the three platform formation again had the lowest excess distance with the penalty of the added aircraft to the formation. Comparing the miss distances for each of the formations reveals an interesting discovery. The miss distances for the optimal maneuvering formation, even

Traffic	Average Miss Distance (ft.)	Standard Deviation (ft.)	Minimum Miss Distance (ft.)
Target 1	1762	39.9	1722
Target 2	7918	53.9	7864
Target 3	5276	59.0	5217
Target 4	2074	33.1	2041

Table 7.11: Average and Minimum Miss Distances and Standard Deviations for System 3 with Conflict Resolution.

with the initial spike in error, were comparable to the miss distances for the three platform formation. For targets one and two, the optimal maneuvering formation had the highest average miss distances of 1799 and 5340 feet as well as the highest minimum miss distances of 1759 and 5281 feet. For targets three and four, the three platform formation had the highest average miss distances of 7963 and 2108 feet. The difference in miss distance between the optimal maneuvering formation and the three platform formation was 60 feet for target two and 20 feet for target four. The miss distances for the orbiting formation were all comparable to the other two formations even with the range error fluctuation.

7.6 Affect of Platform Separation Distance

To determine the affect of separation distance on the range estimate, miss distance, and excess distance traveled, three simulations were run with the separation distance varied by ± 500 feet. The only system tested was that of the one proposed in this research with two measurement platforms maneuvering to take optimal measurements. For each of these simulations, the filter was initialized based on the initial measurements to the target.

7.6.1 Range Error

For the first simulation the platform separation distance was set to 500 feet. Figure 7.16 depicts the averages of the estimated range error for each target. After the maximum average error for target one occurred, the error decreased dramatically to less than 2.5%. The average error for target four decreased below 5% after the first two minutes of the simulation.

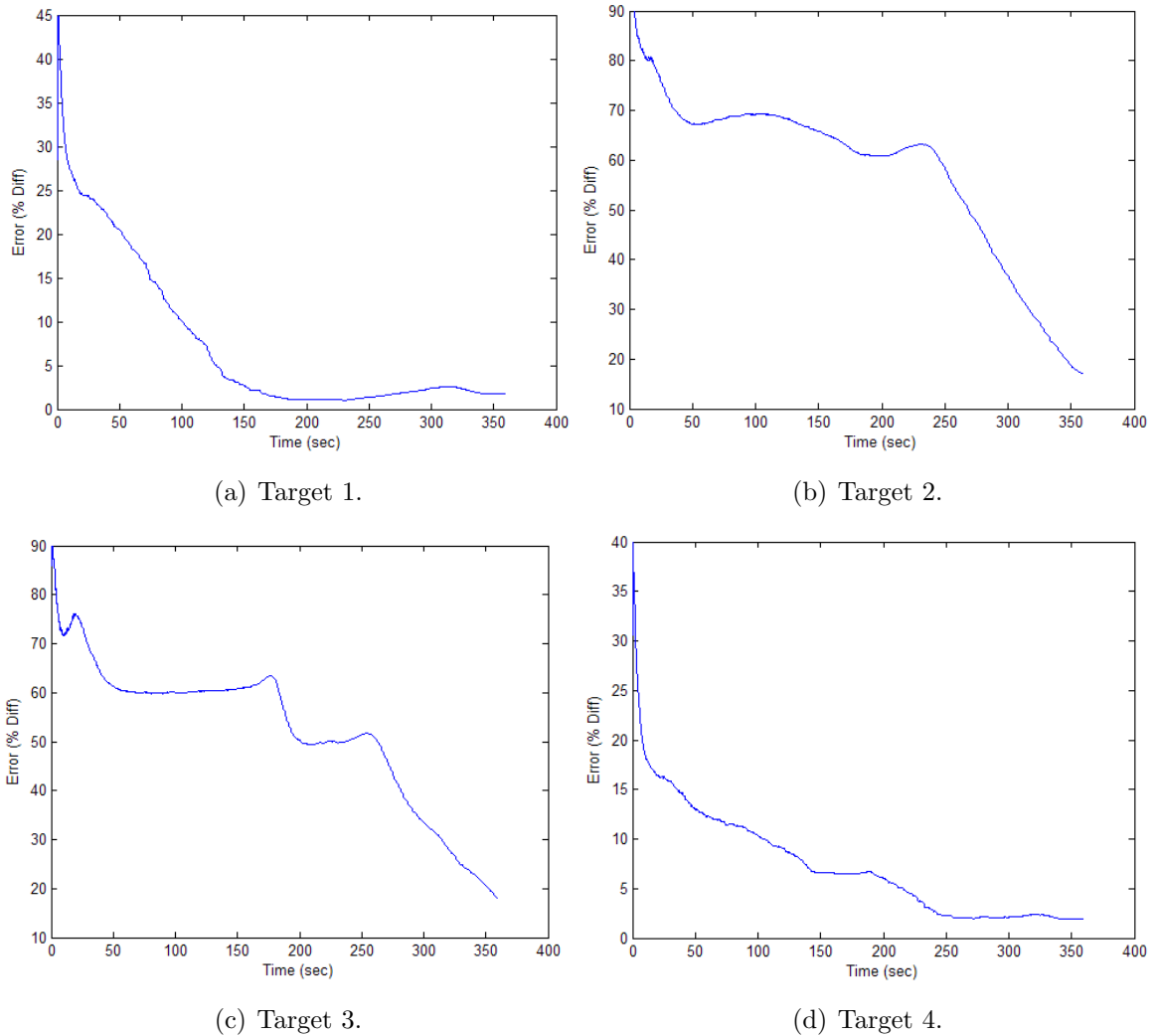


Figure 7.16: Average Range Error with 500 ft. Separation Distance.

For the second comparison simulation (Figure 7.17), the platform separation distance was set to 1000 feet which corresponds to the nominal value.

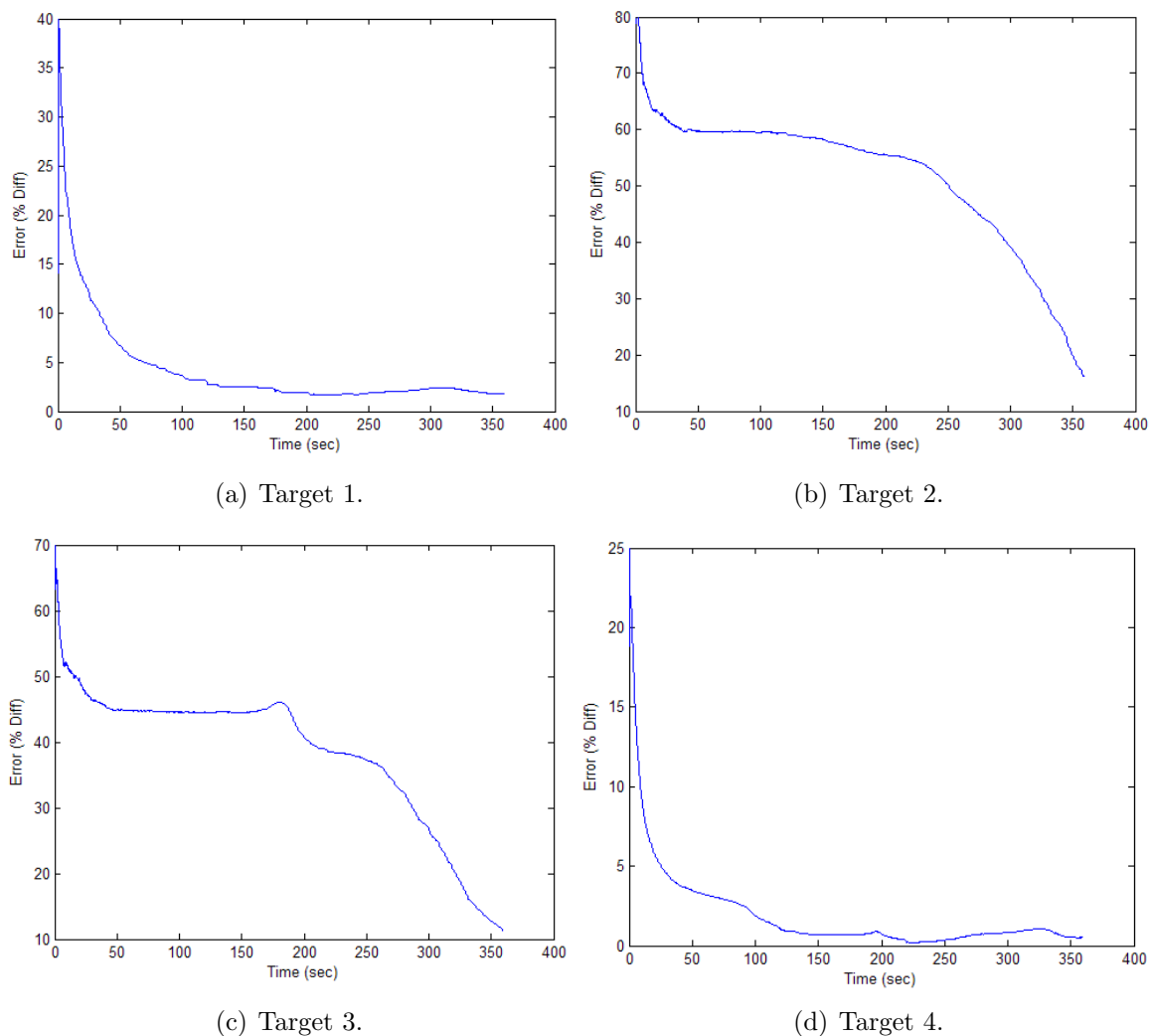
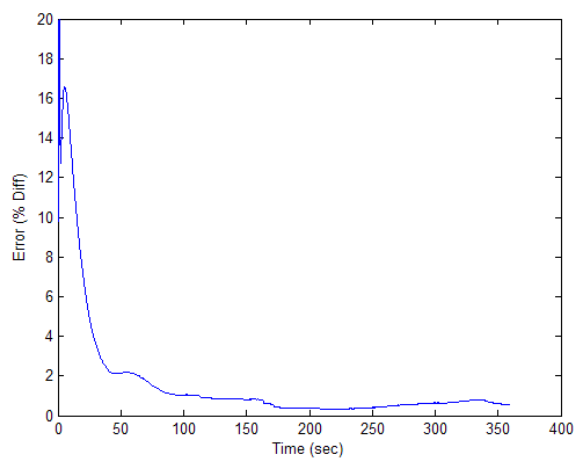
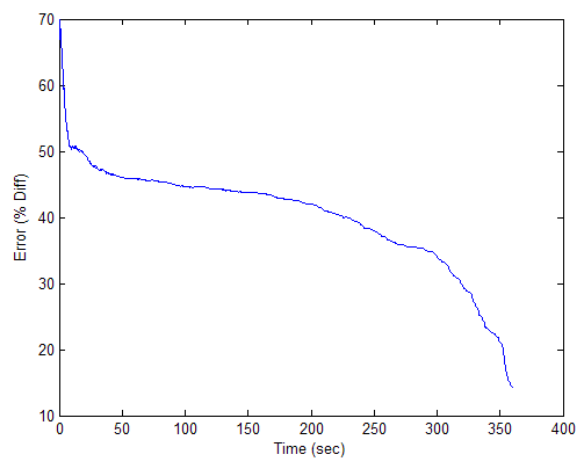


Figure 7.17: Average Range Error with 1000 ft. Separation Distance.

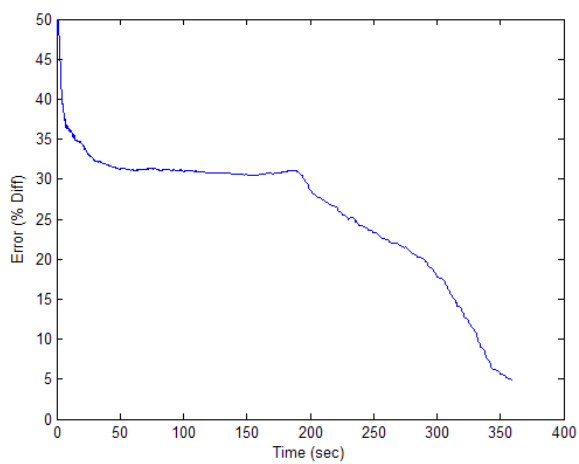
For the next simulation the platform separation distance was set to 1500 feet. Figure 7.18 depicts the averages of the estimated range error for each target. For targets one and four, the error dropped below 1% within the first minute of simulation.



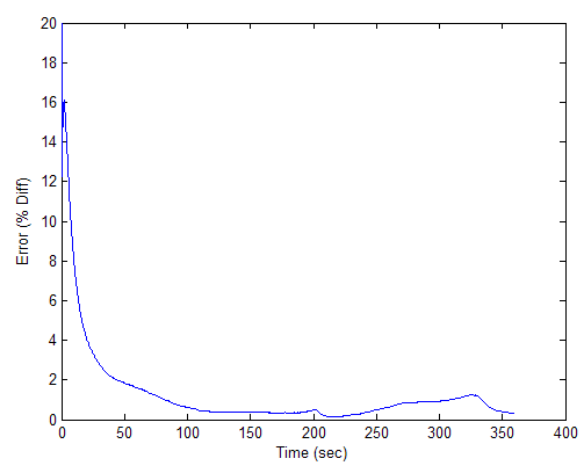
(a) Target 1.



(b) Target 2.



(c) Target 3.



(d) Target 4.

Figure 7.18: Average Range Error with 1500 ft. Separation Distance.

Table 7.12 summarizes the range error comparison for varying separation distances. The formation with the smaller separation distance had larger range error due to the degraded overall measurements when the targets were farther away. The formation with the larger separation distance had lower maximum range error values for each of the four targets.

Formation Description	Target	Minimum Error (%)	Time of Minimum Error (sec)
Optimal Measurement Maneuvering with 500 ft Separation Distance	1	1	180
	2	18	360
	3	18	360
	4	1.5	250
Optimal Measurement Maneuvering with 1500 ft Separation Distance	1	0.2	210
	2	15	360
	3	5	360
	4	0.2	210

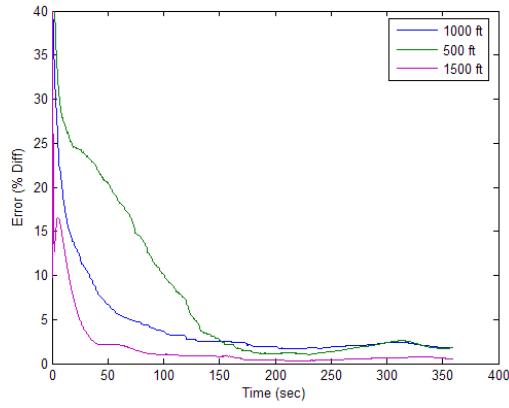
Table 7.12: Summary of Range Error Plots for Varying Separation Distances.

Figure 7.19 depicts the averages of the estimated range error for each of the separation distances. A change in the separation distance had more affect on the range error for targets two and three that are farther away from the platforms.

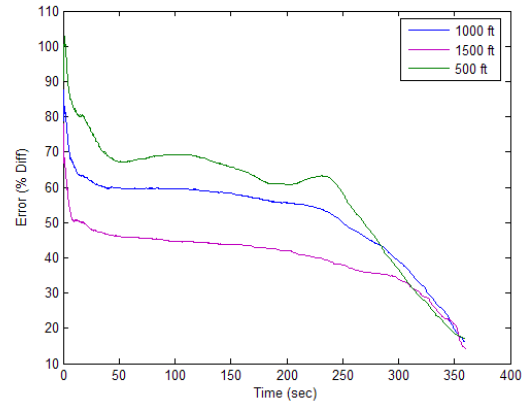
7.6.2 Excess Distance Traveled and Miss Distance

For the system with a separation distance of 500 feet, Table 7.13 summarizes the average percent difference in distance traveled for both measurement platforms as well as the corresponding standard deviations. Table 7.14 lists the average miss distance for each target along with the corresponding standard deviations. On average, platform one traveled 0.18% farther than the straight line distance between its initial and final positions. Platform two traveled an average of 0.14% farther.

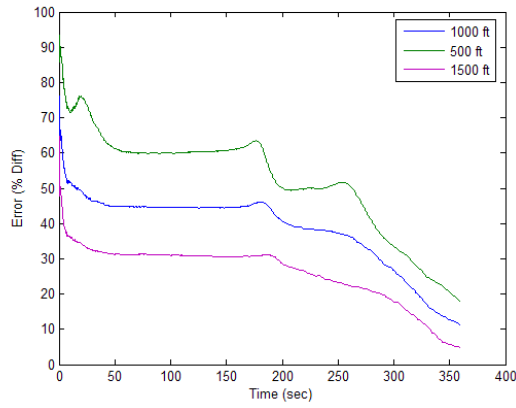
For the system with a separation distance of 1500 feet, Table 7.15 summarizes the average percent difference in distance traveled for both measurement platforms



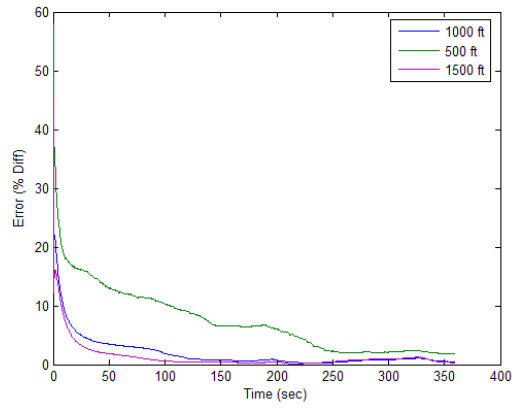
(a) Target 1.



(b) Target 2.



(c) Target 3.



(d) Target 4.

Figure 7.19: Average Range Error Comparison with Varying Separation Distances.

UAS	Excess Distance (% Difference)	Standard Deviation (%)
Platform 1	0.175	0.0456
Platform 2	0.136	0.043

Table 7.13: Average Excess Distance Traveled and Standard Deviation with a Separation Distance of 500 ft.

Traffic	Average Miss Distance (ft.)	Standard Deviation (ft.)	Minimum Miss Distance (ft.)
Target 1	1340	39.3	1300
Target 2	7893	23.6	7869
Target 3	5901	28.5	5873
Target 4	1635	37.5	1598

Table 7.14: Average and Minimum Miss Distances and Standard Deviations with a Separation Distance of 500 ft.

as well as the corresponding standard deviations. Table 7.16 lists the average miss distance for each target along with the corresponding standard deviations. On average, platform one traveled 0.44% farther than the straight line distance between its initial and final positions. Platform two traveled an average of 0.82% farther.

UAS	Excess Distance (% Difference)	Standard Deviation (%)
Platform 1	0.438	0.226
Platform 2	0.817	0.205

Table 7.15: Average Excess Distance Traveled and Standard Deviation with a Separation Distance of 1500 ft.

Traffic	Average Miss Distance (ft.)	Standard Deviation (ft.)	Minimum Miss Distance (ft.)
Target 1	2297	40.4	2257
Target 2	1220	106.5	1114
Target 3	2243	39.5	2204
Target 4	2381	36.3	2345

Table 7.16: Average and Minimum Miss Distances and Standard Deviations with a Separation Distance of 1500 ft.

With a 500 foot increase in separation distance, from 1000 to 1500 feet, the minimum miss distances for targets two and three decreased by more than 2000 feet.

This was more than likely due to a change in the resolution heading caused by the decrease in range error for each of the respective targets. With a 500 foot decrease in separation distance, from 1000 to 500 feet, the excess distance traveled decreased. The downside to this scenario was that the average miss distance also decreased except for target three.

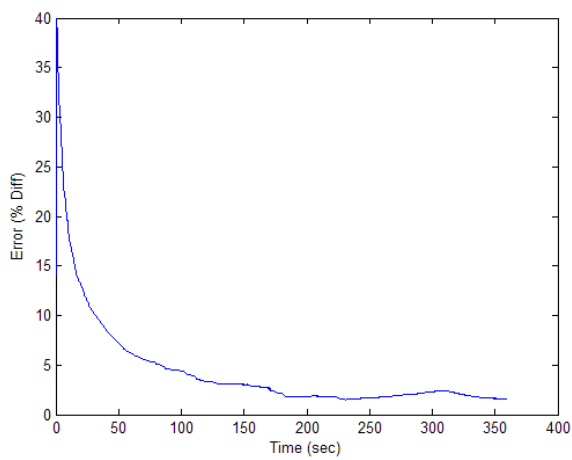
7.7 Affect of UAS Performance Parameters

To determine the affect the UAS performance parameters have on the range estimate, miss distance, and excess distance traveled, two simulations were run. The first with a specific excess power (SEP) of 500 and a maximum rate of turn (ROT) of 90 deg/min. The second with a SEP of 1500 and a maximum ROT of 270 deg/min. The only system tested was that of the one proposed in this research with two measurement platforms maneuvering to take optimal measurements. A platform separation distance of 1000 feet and a miss distance of 2000 feet were used for each simulation. For each of these simulations, the filter was initialized based on the initial measurements to the target.

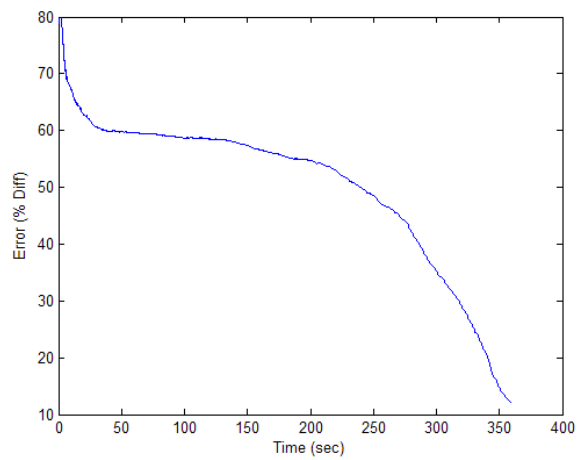
7.7.1 Range Error

For the first simulation, Figure 7.20 depicts the averages of the estimated range error for each target. For targets one and four, after the maximum average range error occurred, the error dropped below 5% within the first minute of simulation.

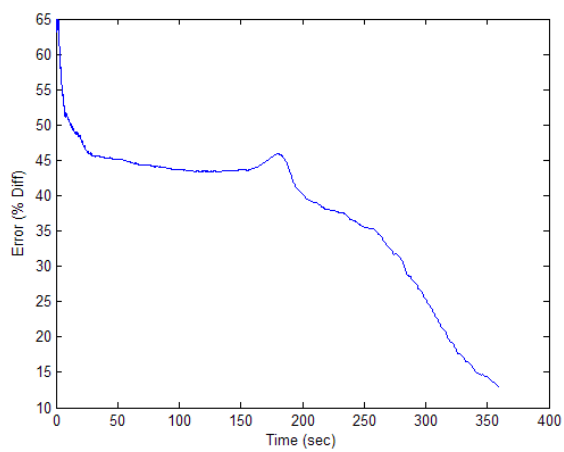
The simulation with the SEP and maximum ROT set to 1000 ft/min and 180 deg/min respectively, was previously presented in Figure 7.17 and represents the nominal performance parameters. For the next simulation the SEP and maximum ROT was set to 1500 ft/min and 270 deg/min respectively. Figure 7.21 depicts the



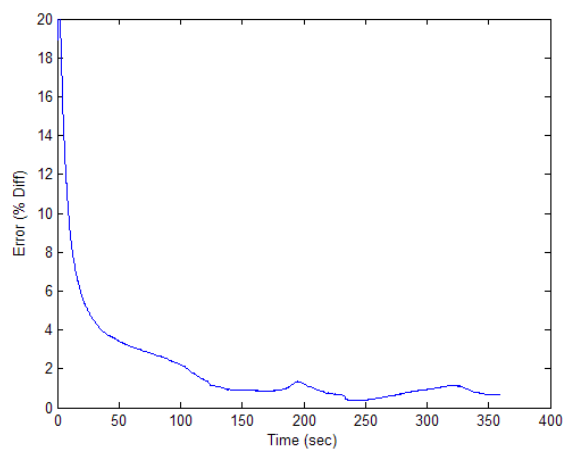
(a) Target 1.



(b) Target 2.



(c) Target 3.



(d) Target 4.

Figure 7.20: Average Range Error with SEP of 500; ROT of 90 deg/min.

averages of the estimated range error for each target. For targets one and four, the range error promptly dropped below 5% within the first 50 seconds of simulation.

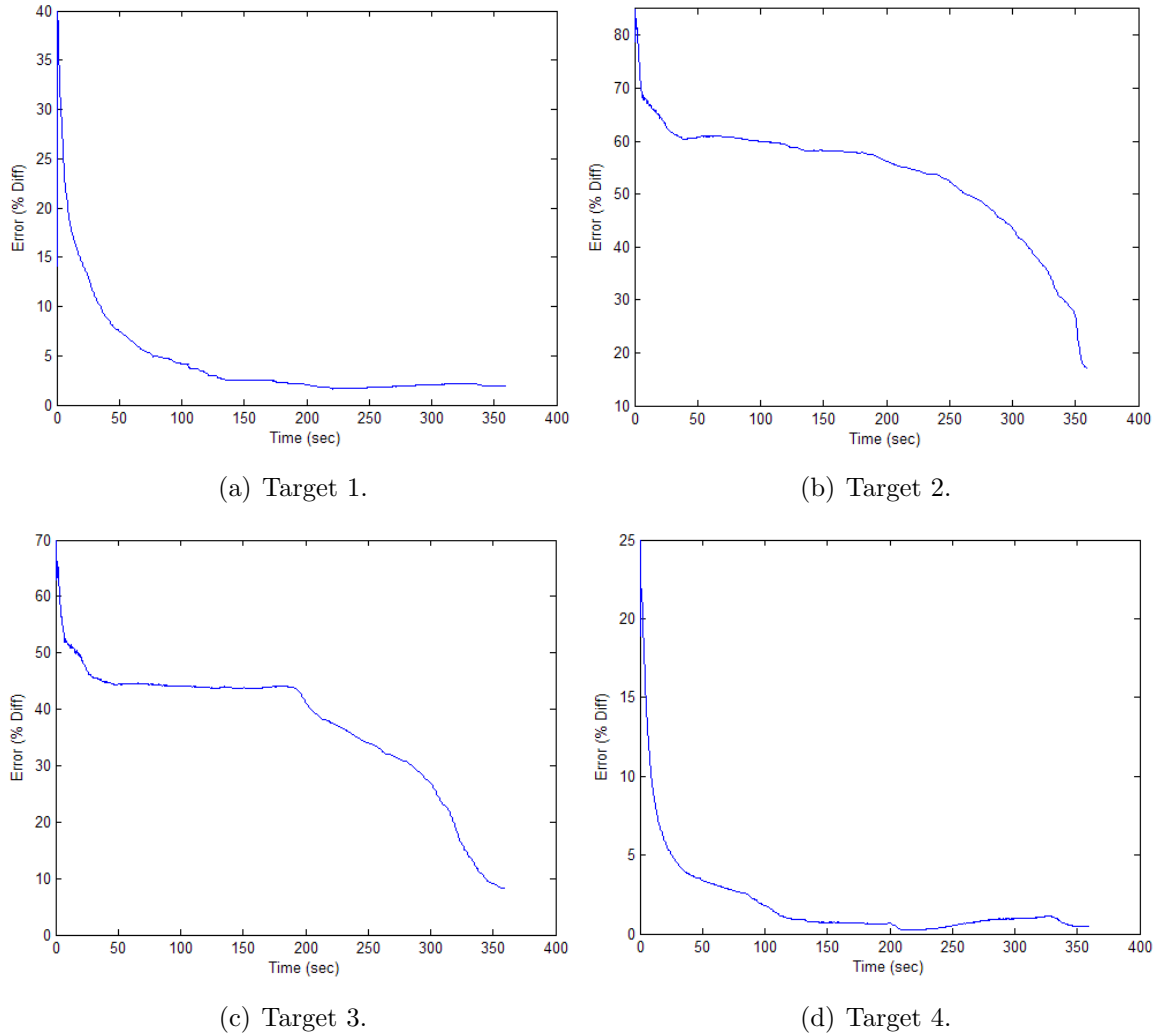


Figure 7.21: Average Range Error with SEP of 1500; ROT of 270 deg/min.

Table 7.17 summarizes the range error comparison for varying UAS performance parameters. Surprisingly, the performance parameters had little effect on the overall range estimates.

Formation Description	Target	Minimum Error (%)	Time of Minimum Error (sec)
Optimal Measurement Maneuvering with SEP of 500 and ROT of 90 deg/min	1	2	170
	2	12	360
	3	12	360
	4	0.2	240
Optimal Measurement Maneuvering with SEP of 1500 and ROT of 270 deg/min	1	2	210
	2	18	360
	3	9	360
	4	0.2	210

Table 7.17: Summary of Range Error Plots for Varying UAS Performance Parameters.

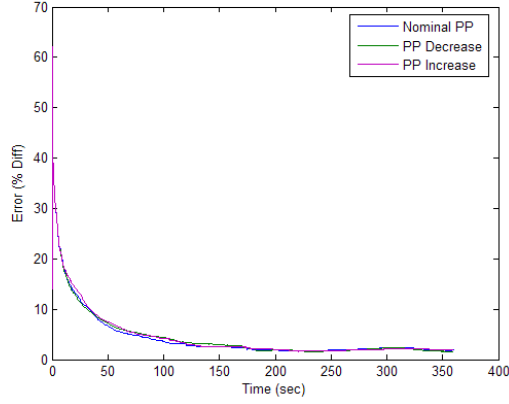
Figure 7.22 depicts the averages of the estimated range error for each of the separation distances. A change in the performance parameters had little affect on the range error.

7.7.2 Excess Distance Traveled and Miss Distance

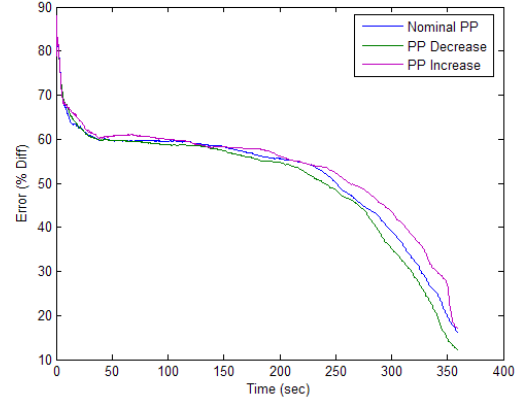
For the system with the SEP and maximum ROT set at 500 and 90 deg/min respectively, Table 7.18 summarizes the average percent difference in distance traveled for both measurement platforms as well as the corresponding standard deviations. Table 7.19 lists the average miss distance for each target along with the corresponding standard deviations. On average, both platforms traveled 0.29% farther than the straight line distance between their initial and final positions.

UAS	Excess Distance (% Difference)	Standard Deviation (%)
Platform 1	0.294	0.104
Platform 2	0.292	0.115

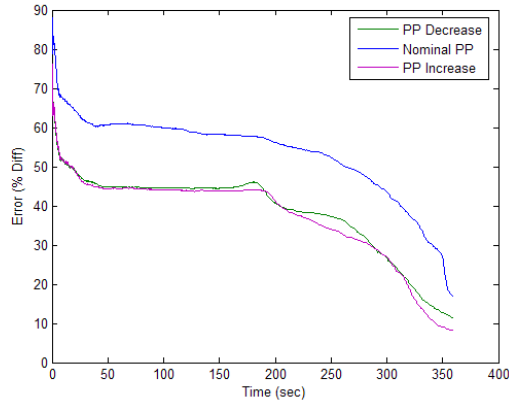
Table 7.18: Average Excess Distance Traveled and Standard Deviation; SEP of 500, ROT of 90 deg/min.



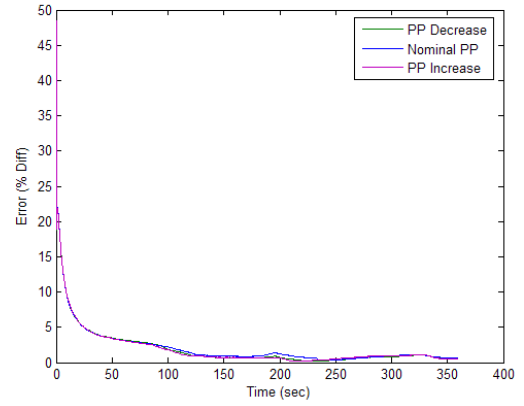
(a) Target 1.



(b) Target 2.



(c) Target 3.



(d) Target 4.

Figure 7.22: Average Range Error Comparison with Varying Performance Parameters.

Traffic	Average Miss Distance (ft.)	Standard Deviation (ft.)	Minimum Miss Distance (ft.)
Target 1	1499	56.9	1442
Target 2	8492	111.5	8381
Target 3	6143	117.1	6026
Target 4	1981	21.0	1960

Table 7.19: Average and Minimum Miss Distances and Standard Deviations; SEP of 500, ROT of 90 deg/min.

For the system with the SEP and maximum ROT set at 1500 and 270 deg/min respectively, Table 7.20 summarizes the average percent difference in distance traveled for both measurement platforms as well as the corresponding standard deviations. Table 7.21 lists the average miss distance for each target along with the corresponding standard deviations. On average, platform one traveled 0.41% farther than the straight line distance between its initial and final positions. Platform two traveled an average of 0.58% farther.

UAS	Excess Distance (% Difference)	Standard Deviation (%)
Platform 1	0.407	0.237
Platform 2	0.583	0.134

Table 7.20: Average Excess Distance Traveled and Standard Deviation; SEP of 1500, ROT of 270 deg/min.

Traffic	Average Miss Distance (ft.)	Standard Deviation (ft.)	Minimum Miss Distance (ft.)
Target 1	1928	22.4	1906
Target 2	1220	213.1	1007
Target 3	1904	288.0	6026
Target 4	1977	28.3	1960

Table 7.21: Average and Minimum Miss Distances and Standard Deviations; SEP of 1500, ROT of 270 deg/min.

With a decrease in performance parameters, the average miss distance for targets one and four decreased. For the other two targets, the miss distances increased slightly. With an increase in performance parameters, the average miss distances for targets two, three, and four decreased. The average miss distance for target one increased approximately 120 feet after the increase in performance.

7.8 Accuracy of Error Bounds

Each target position and velocity estimate from the EKF has an associated area of uncertainty or error bound. To test the accuracy of this error bound, during the simulation in Section 7.2, data was collected on the area of uncertainty to produce a histogram for each target in the simulation. Each histogram shows the number of range estimates that had a certain normalized deviation. Figure 7.23 illustrates a top view of the estimated target positions, in red, as well as the associated error bound on the estimate in green. The blue lines are the two measurement platforms. To illustrate the error bounds, Figure 7.24 depicts a zoomed view of the initial error

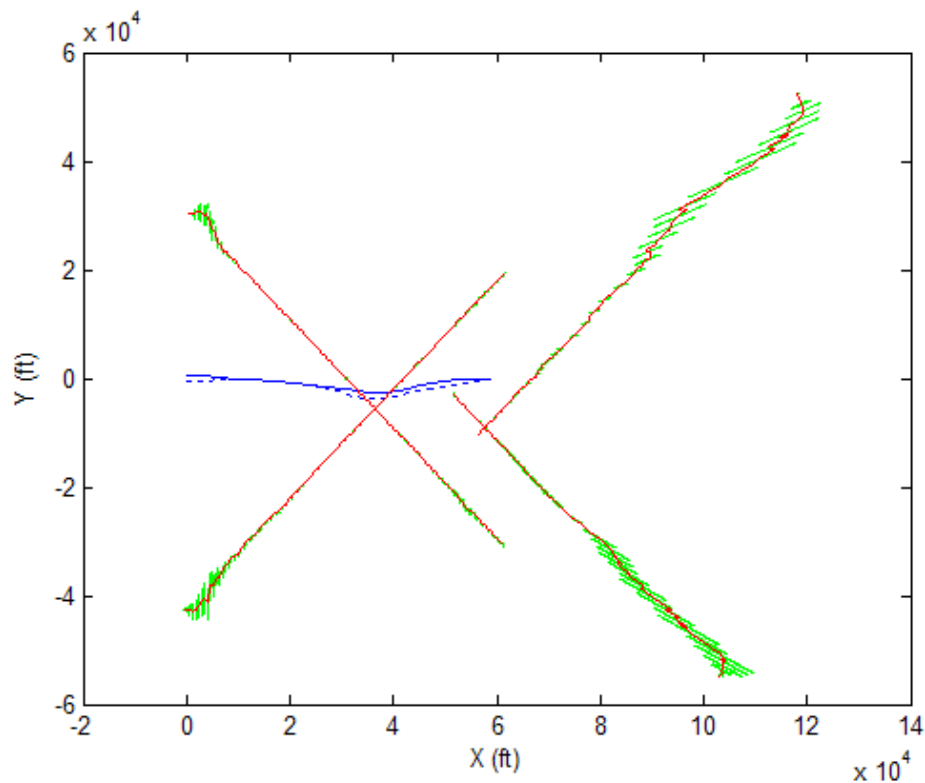


Figure 7.23: Estimated Target Positions with Associated Area of Uncertainty.

bounds for target three, from the lower right corner of Figure 7.23.

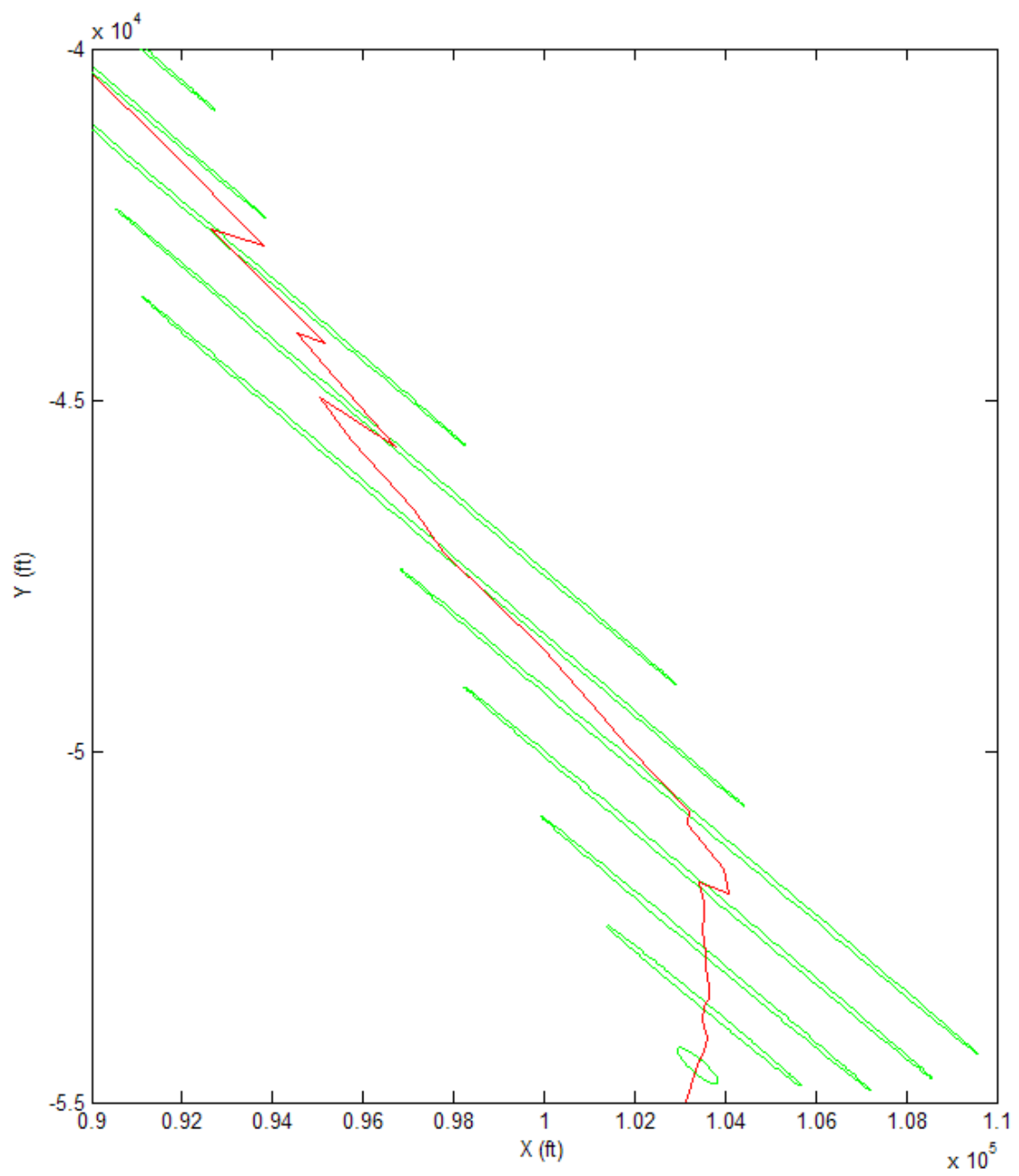


Figure 7.24: Initial Estimated Target Position with Associated Area of Uncertainty for Target 3.

Each range estimate from the EKF has an associated variance. From this variance, the standard deviation for the estimate can be determined. The normal cumulative density function (NCDF) for each value of standard deviation is plotted over the histogram plots to represent a normal distribution. Figure 7.25 depicts the histogram plots for each target.

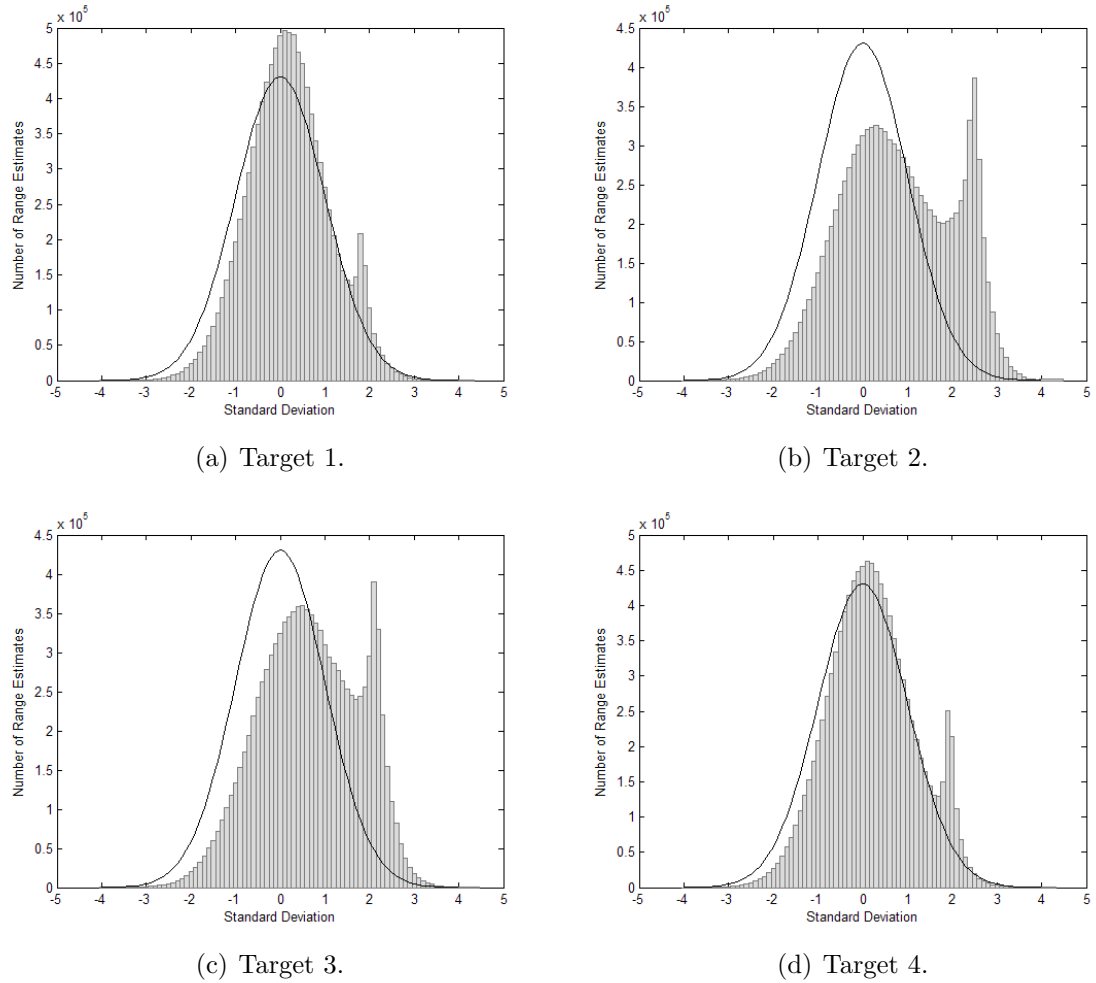


Figure 7.25: Range Estimate Histograms.

The histograms for targets one and four closely follow the normal distribution represented by the NCDF except for a few values of standard deviation. The histogram for target two closely follows the normal distribution represented by the NCDF except

for standard deviation values between two and three. The histogram for target three closely follows the normal distribution represented by the NCDF except for standard deviation values between two and 2.5. The range estimates that do not correspond to a normal distribution are believed to be caused from the error in the filter initialization. Initially, the covariance matrix is set to assumed values. This may be inconsistent with the true error value and would result in errors outside the expected bounds.

7.9 System Reliability

To determine the reliability of the system a random target generator was incorporated into the simulation. For comparison, two simulations of 1000 Monte Carlo iterations each were run. For the first simulation, the number of conflicting air traffic flight paths was randomly selected each iteration having a value of one, two, or three. For the second simulation, the number of conflicting flight paths was held constant at one. For both simulations, the miss distance for conflicting traffic was set to 2000 feet to allow for any inaccurate measurements and to try to ensure a near miss did not occur.

For the first simulation, each iteration contained a random number of targets with random headings and flight speeds. The flight speed was restricted to a minimum of 80 and a maximum of 250 knots. The intercept points for each of the targets was also chosen at random and uniformly distributed along the predicted flight path of the measurement UASs. It was assumed that each target would maintain separation from all other targets at all times. The reliability of the system was determined from the number of near misses that occurred during the simulation. In the end, 128 near

misses had been experienced. This equates to approximately one near miss every eight different target scenarios or a near miss rate of 12.8%.

To determine what scenarios were causing problems for the system, the simulations were set up to store the target geometry in the case of a near miss. In most of the instances when a near miss occurred, it was after two successive targets were approaching the flight path of the platforms approximately 180° apart. This resulted in the platforms being boxed in. As the platforms maneuvered around the first conflict, they had in-turn maneuvered themselves into a worse situation with the second traffic conflict. Once this time had passed, there simply was not enough time remaining for the platforms to maneuver back before the distance between the traffic and platforms was less than 500 feet. Figure 7.26 depicts one such situation where the platforms maneuvered around the first target only to intercept the second. For some of the target scenarios, the error in the estimated range, resulting from the targets being in excess of 10 nautical miles away, caused a delay in determining if the traffic was a conflict. This delay usually resulted in the occurrence of a near miss.

For the last simulation, each iteration contained a new and random target scenario with random headings and flight speeds just as before only with a single target. During this simulation, 37 near misses occurred. This means the simulation had a near miss rate of 3.7%.

After reviewing some of the near miss data from the simulation, it appears the error in range estimate for some of the cases was higher than usual. This high range error made it difficult for the conflict resolution controller to determine an accurate avoidance heading.

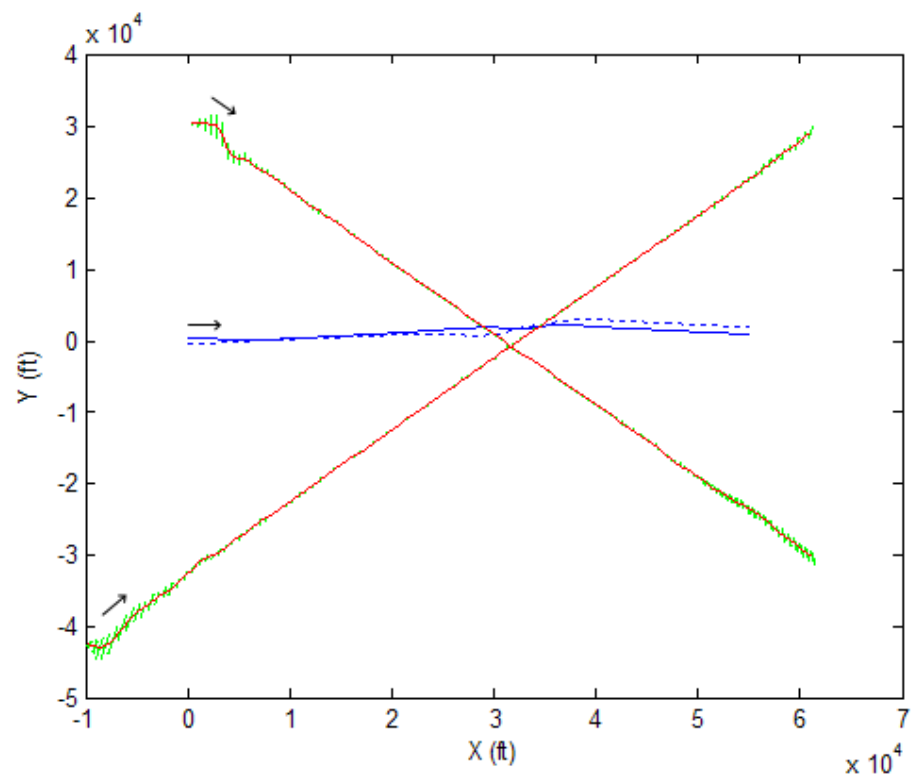


Figure 7.26: Multiple Target Near Miss Scenario.

CHAPTER 8

CONCLUSIONS

Overall, a small, light weight SAA system was simulated. The proposed optimal maneuvering formation was able to perform just as well or better than the comparison formations in terms of average miss distance and minimum miss distance as well as minimum range error for the closest of the four targets. During the time when the targets were closest to the platforms, the optimal maneuvering formation had a lower range error than the orbiting formation. The excess distance traveled for maneuvering caused very little expense in overall distance traveled. The conflict resolution algorithm caused very little degradation in the range estimate.

8.1 Comparison of Platform Separation Distances

When the range error for each of the three separation distances was compared, it was determined that an increase in separation distance provided better range estimates especially for targets that are more than a few miles away. The penalty for this better range estimate however was a decrease in average miss distance for targets two, three, and four.

With a 500 foot decrease in separation distance, the maximum error for each of the targets increased significantly. This was likely due to the degraded overall azimuth measurement as the platforms became closer together. The minimum average error however, was close to the same for each of the different platform separation distances. With the smaller separation distance, the time that the maximum error occurred for

targets two and three, the targets that are the farthest away, also changed. This result indicates the angle of the platforms had different effects for each of the formations.

8.2 Comparison of Performance Parameters

Comparing the range error and excess distance traveled for each of the three sets of UAS performance parameters, it was found that a change in performance parameters changed the range error and excess distance traveled very little. The performance parameters did however affect the average and minimum miss distances.

The major change noticed with a change in performance parameters was in the UAS's ability to maintain their formation size. When the performance parameters were decreased and the formation was commanded to move, a few instances resulted in the platform separation distance growing momentarily. This was caused by the platforms being commanded to a new heading from the conflict resolution controller as well as the angle of the platforms changing to take measurements. The acceleration limits in the controller had been reached and it became a matter of time before the platforms moved to their desired location.

8.3 Error Bound Accuracy

After reviewing the histograms for the range estimates, it was determined that the estimates closely follow a normal distribution except for a few occasions. For targets one and four there are only a few values of standard deviation where the number of range estimates did not follow a normal distribution. This was more than likely associated with the peak in the range error noticed in the beginning of the simulation for each target. This peak in error caused by the error in filter initialization results in range estimates that are not normally distributed for a short

period of time. The remaining range estimates being normally distributed suggests the estimated variance from the EKF and hence the error bounds are accurate after filter initialization.

For targets two and three however standard deviations greater than two have a higher number of range estimates than expected. This is more than likely due to the fact that targets two and three start more than twelve nautical miles away from the platforms. At that distance, the platform's measurement accuracy was degraded. When this measurement degradation was coupled with the initial error from filter initialization mentioned above, a larger number of range estimates become abnormally distributed.

For each target, even those with a larger number of abnormally distributed estimates, the majority of the range estimates were normally distributed. This meant for the majority of the simulation the actual target location was in the predicted area of uncertainty with a 74% confidence with multiple variables considered.

8.4 System Reliability

During the first simulation to determine the system reliability, 128 near misses occurred. For the second simulation, when the platforms were only faced with one traffic conflict each iteration, the near miss rate was decreased by approximately 9% resulting in a total of 37 near misses throughout 1000 different target scenarios. This simulation showed a dramatic improvement in the near miss ratio from the multiple target simulation. It was likely that this was due to the conflict resolution algorithm. The algorithm was originally intended for single target scenarios so adapting it to work with multiple targets proved to be troublesome.

The simulation results proved that indeed the proposed SAA system is a viable solution for the incorporation of UASs into the NAS. Since SAA system requirements are not currently available, the accuracy of the system in terms of reliability is unknown exactly. While the system reliability is not as well as the author would have liked, it is believed that the process described is a good start to a SAA system for implementation on small unmanned aircraft that perform missions at fairly low altitudes during VMC in the NAS. Where the system struggles, is with air traffic that is greater than five nautical miles away. The filter has a difficult time accurately predicting the location of the traffic at this range.

CHAPTER 9

FUTURE WORK

Using the work presented herein as a foundation, the author would like to make several suggestions for future research on using collaborative control for SAA systems. The first would be instead of using multiple sensors on each platform to implement the use of a single gimballed camera to detect and take measurements on conflicting traffic. Another suggestion would be to investigate the use of a third measurement aircraft maneuvering in the system. Also, altitude changes for the measurement aircraft could be added to the control algorithm for conflict resolution as well as the ability to handle multiple targets simultaneously. Lastly, the issue of system reliability should be investigated further to try to increase the reliability of the system by decreasing the number of near misses with other air traffic.

A single gimballed camera could be used in place of the three fixed cameras to monitor the same field of view with the possibility of a weight savings. Instead of each camera covering a specific area around the circumference of the aircraft the single camera would simply scan the FOR from side to side looking for a target. One possible problem with this arises when there are multiple targets in the FOR. This is because as the aircraft maneuver, measurements for all of the targets would not be available at every time step. The measurement values would be intermittent depending on the orientation of the scanning camera. One would need to incorporate this loss of measurement into the EKF and determine the effects on the filter as well as the conflict resolution algorithm.

The addition of a third measurement platform maneuvering in the formation would decrease the time it takes to maneuver the aircraft to take more accurate measurements. This could possibly be used in combination with the gimballed camera to solve the problem with multiple targets. To accomplish this task, modifications to the control algorithm would need to be made to ensure the three UASs did not interfere with each other. This would allow two aircraft to take measurements on one target while the third aircraft took measurements on a separate target.

Altitude changes in the conflict resolution piece of the system could possibly decrease the course deviations necessary for the measurement platforms to remain “well clear” of other air traffic. Included with altitude changes is the ability for the formation to rotate from the aircraft flying abreast to flying over each other at different altitudes. This too could decrease course deviations by decreasing the diameter of the formation. The varying types of formation maneuvers could be applied depending on the predicted flight paths for each target. With the conflict resolution algorithm, the main piece of future work would be to incorporate the ability to simultaneously resolve conflicts with multiple targets. This would possibly decrease the near miss rate for multiple target scenarios.

BIBLIOGRAPHY

- [1] Reynish, W., "UAVs Entering the NAS," *Avionics Magazine*, October 2004, <http://www.aviationtoday.com/av/categories/military/1139.html> [retrieved 28 February 2009].
- [2] Lopez, R., "Avoiding Collisions in the Age of UAVs," *Aerospace America*, June 2002, <http://www.aiaa.org/Aerospace/Article.cfm?issuetocid=223&ArchiveIssueID=27> [retrieved 28 February 2009].
- [3] "Safety of Flight," *Aeronautical Information Manual*, U.S. Department of Transportation, 2009.
- [4] "General Operating and Flight Rules," *Federal Aviation Regulations*, U.S. Department of Transportation, 2009.
- [5] Sabatini, N., "Before the House Committee on Transportation and Infrastructure, Subcommittee on Aviation on Unmanned Aircraft Activities," March 2006, <http://testimony.ost.dot.gov/test/pasttest/06test/sabatini4.htm> [retrieved 20 February 2009].
- [6] "Unmanned Aerial Vehicles Roadmap 2002-2027," Office of the Secretary of Defense, December 2002, http://permanent.access.gpo.gov/websites/dodandmilitaryejournals/www.acq.osd.mil/usd/uav_roadmap.pdf [retrieved 5 January 2009].
- [7] Coulter, D., "UAS Integration into the National Airspace System: Modeling the Sense and Avoid Challenge," AIAA 2009-1926, AIAA Infotech@Aerospace Conference, Seattle, WA, April 2009.
- [8] Shakernia, O., Chen, W.-Z., and Raska, M. V. M., "Passive Ranging for UAV Sense and Avoid Applications," AIAA 2005-7179, AIAA Infotech@Aerospace Conference, Arlington, VA, September 2005.
- [9] Grilley, D. E., "Resolution Requirements for Passive Sense and Avoid," January 2005, http://www.uavm.com/images/GRILLEY_.PDF [retrieved 28 April 2009].
- [10] Ebdon, M. D. and Regan, J., "Sense-and-Avoid Requirement of Remotely Operated Aircraft (ROA)," OPR: HQ ACC/DR-UAV SMO, June 2004, http://www.amtech-usa.org/a5/news/SAAWP_signed.pdf [retrieved 6 May 2009].

- [11] Dennis, A., Archibald, J., Edwards, B., and Lee, D. J., “On-Board Vision-Based Sense-and-Avoid for Small UAVs,” AIAA 2008-7322, AIAA Guidance, Navigation and Control Conference, Honolulu, HI, August 2008.
- [12] Pachter, M., Ceccarelli, N., and Chandler, P. R., “Vision-Based Target Geolocation Using Micro Air Vehicles,” *AIAA Journal of Guidance, Control, and Dynamics*, Vol. 31, No. 3, May-June 2008, pp. 597–615.
- [13] Dobrokhodov, V. N., Kaminer, I. I., Jones, K. D., and Ghabcheloo, R., “Vision-Based Tracking and Motion Estimation for Moving Targets Using Unmanned Air Vehicles,” *AIAA Journal of Guidance, Control, and Dynamics*, Vol. 31, No. 4, July-August 2008, pp. 907–917.
- [14] Effland, J., Seanor, B., Gu, Y., and Napolitano, M., “Application of Machine Vision in Unmanned Aerial Systems for Autonomous Target Tracking,” AIAA 2008-7251, AIAA Guidance, Navigation and Control Conference, Honolulu, HI, August 2008.
- [15] Johnson, E. N., Calise, A. J., Watanabe, Y., Ha, J., and Neidhoefer, J. C., “Real-Time Vision-Based Relative Aircraft Navigation,” *AIAA Journal of Aerospace Computing, Information, and Communication*, Vol. 4, No. 4, April 2007, pp. 707–738.
- [16] “Aircraft Collision Avoidance Systems,” July 2008, http://en.wikipedia.org/wiki/Aircraft_collision_avoidance_systems [retrieved 10 May 2009].
- [17] “TCAS Home Page,” Federal Aviation Administration, November 2007, <http://adsb.tc.faa.gov/TCAS.htm> [retrieved 10 May 2009].
- [18] “Surveillance and Broadcast Services,” Federal Aviation Administration, September 2008, http://www.faa.gov/about/office_org/headquarters_offices/ato/service_units/enroute/surveillance_broadcast/ [retrieved 10 May 2009].
- [19] “Traffic Alert and Collision Avoidance System,” The MITRE Corporation, 2009, http://www.caasd.org/work/project_details.cfm?item_id=153 [retrieved 12 May 2009].
- [20] “Air Traffic Control,” *Aeronautical Information Manual*, U.S. Department of Transportation, 2009.
- [21] Griffith, J. D., Kochenderfer, M., and Kuchar, J., “Electro-Optical System Analysis for Sense and Avoid,” AIAA 2008-7253, AIAA Guidance, Navigation and Control Conference, Honolulu, HI, August 2008.

- [22] Fasano, G., Accardo, D., Moccia, A., Carbone, C., Ciniglio, U., Corrado, F., and Luongo, S., "Multi-Sensor-Based Fully Autonomous Non-Cooperative Collision Avoidance System for Unmanned Air Vehicles," *AIAA Journal of Aerospace Computing, Information, and Communication*, Vol. 5, No. 10, October 2008, pp. 338.
- [23] "Unmanned Aircraft Systems Fact Sheet," Federal Aviation Administration, February 2009, http://www.faa.gov/news/fact_sheets/news_story.cfm?newsId=6287 [retrieved 10 May 2009].
- [24] "SC-203 Unmanned Aircraft Systems," Radio Technical Commission for Aeronautics, 2007, <http://www.rtca.org/comm/Committee.cfm?id=45> [retrieved 10 May 2009].
- [25] Welch, G. and Bishop, G., "An Introduction to the Kalman Filter," July 2006, http://www.cs.unc.edu/~welch/media/pdf/kalman_intro.pdf [retrieved 2 January 2009].
- [26] "PID Controller," 2009, http://en.wikipedia.org/wiki/PID_controller [retrieved 7 April 2009].
- [27] Bilimoria, K. D., "A Geometric Optimization Approach to Aircraft Conflict Resolution," AIAA 2000-4265, AIAA Guidance, Navigation and Control Conference, Denver, CO, August 2000.
- [28] Paielli, R. A., "Algorithms for Tactical and Strategic Conflict Resolution," AIAA 2001-7910, AIAA Technology, Integration, and Operations Forum, Los Angeles, CA, October 2001.
- [29] Bach, R., Farrell, C., and Erzberger, H., "An Algorithm for Level-Aircraft Conflict Resolution," 2007, http://www.aviationsystemsdivision.arc.nasa.gov/publications/tactical/bach_05_07.pdf [retrieved 25 May 2009].